Multiscale investigation of quasi-brittle fracture characteristics in a 9Cr-1Mo ferritic-martensitic steel embrittled by liquid lead-bismuth under low cycle fatigue

Reference:

Gong Xing, Marmy Pierre, Volodin Alexander, Amin-Ahmadi Behnam, Schryvers Dominique, et al..- Multiscale investigation of quasi-brittle fracture characteristics in a 9Cr-1Mo ferritic-martensitic steel embrittled by liquid lead-bismuth under low cycle fatigue

Corrosion science - ISSN 0010-938X - 102(2016), p. 137-152

Full text (Publishers DOI): http://dx.doi.org/doi:10.1016/j.corsci.2015.10.003

Multiscale investigation of quasi-brittle fracture characteristics in a 9Cr-1Mo ferritic-martensitic steel embrittled by liquid lead-bismuth under low cycle fatigue

Xing Gong [a,b,*], Pierre Marmy [a], Alexander Volodin [d], Behnam Amin-Ahmadi [c], Ling Qin [b], Dominique Schryvers [c], Serguei Gavrilov [a], Erich Stergar [a], Bert Verlinden [b], Martine Wevers [b], Marc Seefeldt [b]

[a] SCK•CEN (Belgian Nuclear Research Centre), Boeretang 200, B-2400 Mol, Belgium
[b] Department of Materials Engineering (MTM), KU Leuven, Kasteelpark Arenberg 44, Box 2450, B-3001 Heverlee, Belgium
[c] Electron Microscopy for Materials Science (EMAT), University of Antwerp, Groenenborgerlaan 171, Antwerp B2020, Belgium
[d] Laboratory of Solid-State Physics and Magnetism, KU Leuven, Celestijnenlaan 200 D, BE-3001 Leuven, Belgium

*Corresponding author

Email addresses:
gongxingzfl@hotmail.com (X. Gong);
pmarmy@sckcen.be (P. Marmy);
Marc.Seefeldt@mtm.kuleuven.be (M. Seefeldt)

Tel: +32 14 33 3162

Abstract

Liquid metal embrittlement (LME) induced quasi-brittle fracture characteristics of a 9Cr-1Mo ferritic-martensitic steel (T91) after fatigue cracking in lead-bismuth eutectic (LBE) have been investigated at various length scales. The results show that the LME fracture morphology is primarily characterized by quasi-brittle translath flat regions partially covered by nanodimples, shallow secondary cracks propagating along the martensitic lath

boundaries as well as tear ridges covered by micro dimples. These diverse LME fracture features likely indicate a LME mechanism involving multiple physical processes, such as weakening induced interatomic decohesion at the crack tip and plastic shearing induced nano/micro voiding in the plastic zone.

Keywords:

A. Steel

B. AFM

B. SEM

B. TEM

C. LME

1. Introduction

Liquid metal embrittlement (LME) has been reported to occur in a wide variety of solid metal/liquid metal couples, characterized by loss of ductility and fracture toughness of normally ductile metallic materials when stressed in a specific liquid metal environment [1-5]. Since this phenomenon was first discovered about one century ago, extensive investigations have been conducted to study its characteristics and to understand the mechanism, but the essence of LME, particularly on atomic scale, is still in dispute [6-8]. So far, some promising LME models and mechanisms have been proposed, including adsorption induced reduction in surface energy [9], adsorption induced reduction in interatomic cohesion [10, 11], adsorption induced dislocation emission [8, 12-14], grain boundary penetration [15, 16], stress assisted dissolution-condensation [17, 18] and

adsorption enhanced work hardening [19]. The adsorption induced reduction in surface energy mechanism postulates that the surface energy of a solid metal is reduced by adsorption of a liquid metal, thereby lowering the stress required to fracture the solid. The adsorption induced reduction in interatomic cohesion model, to some extent, is equivalent to the adsorption induced reduction in surface energy mechanism. This model claims that the adsorption of liquid metal atoms at crack tips weakens the atomic bonds being in contact with the liquid metal so as to cause interatomic brittle decohesion. The adsorption induced dislocation emission mechanism was proposed to account for the formation of micro dimples observed on LME fracture surfaces. The basic assumption of this mechanism is that adsorption of embrittler atoms at crack tips reduces the shear strength of interatomic bonds, which facilitates dislocation emission at the crack tips and then leads to ductile failure by highly localized plasticity. The two grain boundary penetration models report that grain boundary penetration of liquid metal atoms by atomic diffusion is necessary for LME crack initiation and propagation. The stress assisted dissolution-condensation model hypothesizes that dissolution of a solid in a liquid can be enhanced by an applied stress. As a result, the stress distribution around crack tips creates a gradient of chemical potential, which causes a diffusion flux directing from the crack tips towards the liquid, accompanied by re-condensation of the dissolved solid at the crack walls behind the crack tips. Similar to the adsorption induced dislocation emission mechanism, the adsorption enhanced work hardening mechanism also agrees that adsorption of embrittling atoms at crack tips promotes dislocation emission. However, the difference is that the consequence of the favored dislocation emission in the adsorption enhanced work hardening mechanism is to enhance work hardening at a surface layer around the crack tips,

instead of to create immediate crack propagation as assumed by the adsorption induced dislocation emission mechanism. Then, brittle cracking occurs through the hardened surface layer around the crack tip. Since none of these models and mechanisms is able to provide a unified explanation for all the solid metal/liquid metal embrittling systems discovered so far, to completely figure out the underlying mechanism of LME is still a challenging task [6-8].

Recently, the LME phenomenon of the T91/LBE couple has aroused great interest in the nuclear industry, because of the potential application of T91 steel in the GenIV liquid Pb-Bi cooled nuclear reactors [20-41]. For instance, the excellent swelling resistance under fast neutron flux and superior high temperature mechanical properties enable this steel to be a candidate material to construct the proton beam window of the accelerator driven system (ADS) based MYRRHA nuclear facility, which is being developed at SCK•CEN, Belgium for transmuting long-lived nuclear waste [42]. However, one barrier to qualify this steel for safe use in the MYRRHA reactor is that LME may pose a threat to the structural integrity of the proton beam window by involving premature brittle failure [20-41]. In order to take effective measures to mitigate and prevent the LME risk, the underlying mechanism of this intricate embrittlement phenomenon must be resolved.

Over the past decade, extensive work has been performed to investigate the LME characteristics of T91 steel in LBE environment under different conditions, with special attention to the impact of various parameters on the embrittlement susceptibility, including temperature [21-23, 26, 43, 44], strain rate/loading rate [21, 24, 33], metallurgical state [26, 43], oxygen concentration in LBE [29], pre-exposure treatment [21, 45], surface oxides [45, 46], surface flaws or notches [22], etc. Some important results have been obtained. For

example, LME occurred only in a certain temperature domain, called “ductility trough” [22, 26, 33, 43, 47]. A slow strain rate in conjunction with a low oxygen concentration of LBE were shown to enhance the LME susceptibility of T91 steel [29]. Tempering at a relatively low temperature to harden the steel was also reported to intensify the LME severity [26, 43]. The effect of pre-exposure treatment was demonstrated to rely on oxygen concentration of LBE. Pre-exposure to an oxygen-saturated LBE resulted in the formation of double-layer protective oxides (magnetite and Fe-Cr spinel [48-50]) on the steel surface, thereby reducing the LME effect due to the fact that the crack initiation process was inhibited by the oxide films [45, 51]. On the other hand, pre-exposure to an oxygen-depleted LBE led to dissolution of the protective oxides, which improves the wettability and facilitates the crack initiation [45, 51]. In addition, the presence of stress concentrators such as surface cracks, flaws and notches was observed to greatly favor the occurrence of LME in the T91/LBE system [22]. Unfortunately, a clear explanation of these experimental observations is missing. This can partly be attributed to the great difficulty in clarifying the correlation between the complex microstructure of T91 steel and the LME fracture morphology.

After T91 is cracked in LBE under monotonic loading, transgranular “flat” and “featureless” fracture surfaces have been observed by conventional scanning electron microscopy (SEM) in most of the previous investigations [30, 31, 34, 41, 51]. These observed fractographic features are usually considered as typical manifestations of LME for the T91/LBE system. To describe these complex fracture modes formed under the influence of LBE, the terminology “quasi-cleavage” has been widely used to indicate likely a mixture of prevalent transgranular (or translath) brittle features and limited ductile features. However, using focused-ion beam (FIB) to extract thin foils beneath the fracture surface for

subsequent transmission electron microscopy (TEM) observations, Martin et al. [52] and Hémery et al. [53] have recently obtained different results in T91 steel tested in liquid LBE, liquid indium and liquid sodium environments under monotonic loading. They found that the fracture mode of the secondary cracks emanating from the fracture surfaces was mainly intergranular cracking either at the prior-austenite grain boundaries or at the martensite lath boundaries, rather than transgranular or translath "quasi-cleavage". Based on this interesting finding, they finally proposed not to use "quasi-cleavage" to describe the LME fracture morphology of T91 steel. Hémery et al. [54] even observed intergranular failure in a Fe18Cr9Ni1Mn stainless steel/liquid sodium system. Their observations seem to be supported by a series of LME cases involving evident intergranular penetration of liquid metal atoms, such as polycrystalline Al/liquid Ga [55-58], Ni/liquid Bi [59, 60], Cu/liquid Bi [61] and ferrite iron/liquid zinc [62]. Nevertheless, in our recent work [41], using high resolution electron backscatter diffraction (EBSD), transgranular cracking by cutting either through the prior-austenite grain boundaries or through the martensite lath boundaries was observed to dominate the propagation behavior of the main crack of T91 steel under low cycle fatigue in LBE at 350 °C. This means that the main fatigue crack has a different propagation behavior from the secondary cracks. In this regard, how to properly depict the LME fracture features of T91 steel and especially to interpret the underlying mechanism of their formation is still an open issue. One of the key approaches to deal with this issue could be to examine the LME fracture surface and the microstructure immediately beneath it under very high magnification, considering that the fracture morphology represents the history of the crack tips and LME is a surface phenomenon involving direct microstructural changes only within a very thin layer of material in contact with the liquid metal. Fatigue is

the most important origin of engineering failure, therefore, the main focus of this study is on fatigue fracture surfaces after testing in LBE.

In order to get deeper insights into the nature of the LME phenomenon in the T91/LBE couple, a systematic multiscale microstructural investigation has been performed to characterize the fracture surface of T91 steel cracked in low oxygen LBE under low cycle fatigue and the deformation microstructure immediately beneath it by means of multiple advanced characterization techniques. These techniques include high resolution SEM, atomic force microscopy (AFM), high resolution EBSD and FIB sampling technique for subsequent TEM observations. The observed results are discussed in the framework of the previous literature models and mechanisms. Some new viewpoints are also proposed for a better understanding of the LME mechanism of the T91/LBE couple.

2. Experimental

2.1 Material

The material used in this study was T91 steel. This steel was austenitized at 1050°C for 15 min and then water quenched, followed by tempering at 770°C for 45 min and then air cooling. The chemical composition of the steel is C: 0.097, Cr: 8.87, Ni: 0.12, Mo: 0.87, Mn: 0.39, V: 0.19, Si: 0.22, Nb: 0.08, N: 0.044 and Fe in balance (wt.%).

2.2 Low cycle fatigue test in LBE and vacuum

Low cycle fatigue tests with strain amplitudes of 0.26 to 1.05% were performed under a strain-controlled mode with a Limets3 system [51, 63, 64] in a stagnant LBE

environment at 250, 350 and 400°C. A symmetrical push–pull mode with a triangular waveform was employed (i.e. the strain ratio *R* is -1). The frequency was varied from 0.1 to 0.45 Hz to keep a constant strain rate of 4.5×10^{-3} s^{-1} for all the fatigue tests. Cylindrical specimens with 3.2 mm diameter and 7 mm gauge length were used and the specimen surface was polished up to diamond paste with a particle size of 3 μm. The fatigue system is equipped with a mechanical extensometer to allow for measuring strain at the gauge of a fatigue specimen immersed in LBE. Reference fatigue tests were conducted under a high vacuum condition (vacuum = 10^{-5} to 10^{-6} mbar). The number of cycles to failure (N_f) is defined as the number of cycles when the stress drops by 15% with respect to the stress saturation part.

2.3 Monitoring dissolved oxygen concentration in LBE

During the fatigue test, the dissolved oxygen concentration in LBE was monitored by potentiometric oxygen sensors. The sensors are fabricated with oxygen ion permeable solid electrolyte typically made of yttria partially stabilized zirconia (YPSZ). This solid electrolyte separates the reference electrode (e.g. Bi/Bi_2O_3 or Cu/Cu_2O) from the working electrode (LBE), allowing only oxygen ions to pass through it. The measuring process is based on the potential measurement method at null current in a galvanic cell. The Bi/Bi_2O_3 sensors [65] were used to measure the oxygen concentration in LBE above 300°C, whereas the Cu/Cu_2O sensors [66] were employed to perform oxygen measurements above 200 °C.

The difference of oxygen activity at the reference and working electrode generates an electromotive force (emf, *E*), which can be represented by the Nernst equation

$$E = \frac{RT}{2F} \ln\left(\frac{a_{o,ref}}{a_{o,w}}\right) \quad (1)$$

where R is the gas constant (8.3145 $J \cdot K^{-1} \cdot mol^{-1}$), T is the absolute temperature, F is the Faraday constant (96485.34 $C \cdot mol^{-1}$), $a_{o,ref}$ is the oxygen activity at the reference electrode and $a_{o,w}$ is the oxygen activity at the working electrode (LBE). Inserting the oxygen activity of the reference electrode and activity coefficient of oxygen in LBE into Eq.(1), one can derive the following two equations to calculate the oxygen concentration in LBE:

For the Bi/B_2O_3 sensor [65],

$$E = -0.34756 + 2.5217 \cdot 10^{-4} T - 4.3086 \cdot 10^{-5} T \ln C_O \quad (2)$$

For the Cu/Cu_2O sensor [66],

$$E = -2.2233 \cdot 10^{-1} + 1.3561 \cdot 10^{-4} \cdot T - 4.3087 \cdot 10^{-5} \cdot T \cdot \ln C_O \quad (3)$$

In this study, the oxygen concentration of LBE at 250, 350 and 400 °C measured by the oxygen sensors was 1.28×10^{-7} wt.%, 6.0×10^{-10} to 2.88×10^{-8} wt.% and 8.2×10^{-9} wt.%, respectively.

2.4 Microstructure characterization

After fatigue fracture in LBE, the LBE deposits on the fracture surfaces were cleaned with a chemical solution consisting of CH_3COOH, CH_3CH_2OH and H_2O_2 with a volume ratio of 1:1:1. Then, the fracture surfaces were examined with a JEOL JSM-6610LV SEM with a LaB_6 or W filament operated at 15 kV for low magnification analyses, while high resolution fractographic micrographs were taken using a FEI Helios Nanolab

650 SEM/FIB instrument. The fracture surface was further examined by AFM using a Digital Instruments Dimension 3100 microscope operated in a tapping mode.

The crystallographic orientations along the crack walls were measured using the high resolution EBSD technique (FIB nova 600 nanolab). The EBSD samples were ground with different sand papers in the order of P800, P1200, P2000 and P4000. The samples were then polished by two diamond pastes: 3 microns for 3 min and 1 micron for 5 to 8 min, followed by final polishing for 15 min with an OPS (colloidal silica in suspension) solution containing 40 nm silicon oxides. In order to resolve the fine martensitic lath structure, a small scan step of 20 to 50 nm was used for the EBSD characterization.

TEM thin foils were extracted from site-specific locations of the fracture surface using the FIB lift-out technique with the FEI Helios Nanolab 650 SEM/FIB instrument, enabling the examination of deformation microstructures immediately beneath the fracture surface. During the FIB lift-out from the fracture surface, platinum (Pt) was slowly deposited on the location of interest to preserve the corresponding fracture surface at that location and the microstructure below it. TEM observations of the thin foils were then conducted in the JEOL 3010 scanning TEM operated at an accelerating voltage of 300 kV. In all cases, the TEM images have been selected so as to show the highest dislocation density, as checked by tilting the sample.

The crystallographic orientation around the nanoscale dimples was investigated by automated crystal orientation mapping in TEM (ACOM-TEM) using a FEI Tecnai microscope equipped with a field emission gun and operated at 200 kV. This technique uses small probe diffraction spot patterns in TEM and is an effective method for mapping phase and crystal orientation at the nanoscale. A selected area is scanned with a small probe

(≈2 nm) and the electron diffraction spot patterns are collected using an external Charge-Coupled Device camera. Off-line, every diffraction pattern is compared to the pre-calculated templates of selected phases and the best match is selected.

The high resolution SEM fractography and AFM topography for detecting the nanodimples were performed at the regions corresponding to the last cycle of a fatigue test. Every fatigue test was automatically stopped in the tension phase of the last cycle, when a defined failure criterion was fulfilled. Therefore, no significant compression and crack closure are expected to have happened to that part of the fracture surface examined by SEM and AFM.

3. Results

3.1 As-received microstructure

The initial microstructure of T91 steel was characterized by a combination of optical microscopy (OM), EBSD and TEM, as shown in Fig. 1. It can be seen from Fig. 1a that tempered martensite lath structures are present in the material. The EBSD orientation map in Fig. 1b shows that very fine martensitic laths are embedded in the prior-austenite grains. Most of the laths have low angle grain boundaries (Fig. 1c). TEM bright-field images in Fig. 1(d, e) show that the martensitic lath boundaries are decorated with small precipitates (<500 nm) and dislocation tangles are distributed within some of the laths. The width of the laths varies from 0.2 to 1 μm. The description of the main microstructure of T91 steel is schematically illustrated in Fig. 1f. The prior austenite grains, formed in the

normalizing heat treatment, contain several packets of laths which are produced during the martensitic phase transformation. The packets are composed of a few blocks of laths and $\{111\}_\gamma$ is the habit plane of these laths [67, 68]. The martensitic laths sit inside the blocks. During the tempering heat treatment, carbon atoms in the super-saturated matrix precipitate preferentially at the prior-austenite grain boundaries and the lath boundaries to form fine carbides.

3.2 Effect of LBE on fatigue endurance of T91 steel

As shown in Fig. 2, the low oxygen LBE environment reduces the fatigue lives of T91 steel at 250, 350 and 400°C by a factor of 3 to 10, compared to vacuum. The substantial fatigue life reduction indicates the occurrence of LME and a deleterious effect of LBE environment on the fatigue endurance of T91 steel.

3.3 Fractography and deformation microstructure of T91 steel embrittled by LBE

3.3.1 High-resolution SEM fractography

The fracture surfaces of T91 steel after LBE embrittlement show diverse fracture features, as presented in Figs. 3 and 4. For instance, Fig. 3a displays an overview of the LME fracture surface containing typical “quasi-brittle” cracking features as well as many tear ridges (marked with arrows) being oriented approximately along the fatigue crack propagation direction. Higher magnification SEM micrographs in Fig. 3(b, c) further reveal that numerous submicron “mounds” are distributed on these tear ridges. Most likely, these

small “mounds” are submicron dimples, since the presence of the tear ridges is a typical manifestation of plastic deformation. Occasionally, much larger dimples with a size of 15 μm can be observed on the LME fracture surface, as one example shown in Fig. 3d. More interestingly, microdimples are also present on the intergranular facets (Fig. 3e), indicating that the LME-induced intergranular decohesion involves a certain amount of plastic deformation.

Despite of these ductile features, the prevalent fracture features after testing in LBE appear to be brittle, as evidenced by the frequently observed tiny secondary cracks and flat “featureless” regions in Fig. 4(a, b). The secondary cracks seem to propagate along the martensite lath boundaries (Fig. 4c), since the distances between two neighboring secondary cracks vary from 0.4 to 1.2 μm, which are comparable to the width of the martensite laths determined by the TEM observations in Fig. 1(d, e). It can be deduced, therefore, that these secondary cracks are just located at the lath boundaries. A similar result has also been obtained by Martin et al. [52]. Most likely, the formation of the quasi-brittle flat “featureless” regions enclosed by the secondary cracks is a result of translath cracking. More interestingly, under very high magnifications, Fig. 4(d, e) presents that the flat and “featureless” regions are not perfectly “flat” and “featureless”. Instead, these regions are undulated and covered by a large number of tiny “mounds”. The size of the “mounds” is approximately 30 nm, which is much smaller than that of the “mounds” located on the tear ridges as shown in Fig. 3c. These nanoscale “mounds” could be referred to as nanodimples, since such a kind of tiny ductile features have also been observed by S.P. Lynch in some other solid metal/liquid metal systems using a TEM replica technique [8, 12-14]. Moreover, Neeraj et al. [69] and Martin et al. [70] have also detected similar

features in the fracture surfaces of hydrogen-embrittled steels using high resolution SEM and AFM. In their studies, the detected tiny fracture features have been described as being "mounds". Neeraj et al. [69] were able to demonstrate the observed "mounds" or "undulations" are indeed nanodimples. Their conclusion is an important reference for properly describing the "mounds" observed in this study, since hydrogen embrittlement is very similar to LME in terms of the intrinsic mechanisms [8]. Nevertheless, not all the flat regions are clearly decorated with nanodimples. For instance, Fig. 5(a-c) shows flat regions that are undulated, but where much less nanodimples are present.

To compare the differences between the quasi-brittle fracture surface produced in LBE and the cleavage created under low temperature, high resolution SEM micrographs were also taken from a T91 specimen fractured in liquid nitrogen and the fracture morphology is presented in Fig. 6. Clear distinctions can be differentiated from the LME fracture surface. Fig. 6a presents more evident river patterns and a much smaller number of secondary cracks. A higher magnification picture in Fig. 6b does not reveal any obvious nanodimples on the fracture surface. It should be mentioned here that this SEM fractography was performed after the low temperature fracture surface was exposed to the chemical solution used to clean the LBE deposits. Thus, the absence of the nanodimple-like features on this low temperature fracture surface indicates that the LBE cleaning process did not strongly modify the appearance of the fracture surface by introducing artifacts, such as corrosion pits.

3.3.2 AFM topography of fracture surfaces

To confirm the observation of the nanodimple-like features presented in Fig. 4(d, e), AFM was used to further detect potential tiny features on the flat areas of the LME fracture surface as well as to compare the differences with the low temperature brittle fracture features.

The AFM topographic image of the low temperature brittle fracture surface is shown in Fig. 7a. Similar to the high resolution SEM observation in Fig. 6, no nanoscale undulated features can be observed (see the inset in Fig. 7a). In contrast, the fracture surface created in LBE is highly undulated and nanoscale "mounds" with 20 to 30 nm wide and 1 to 3 nm deep can be clearly identified (Fig. 7b). Since the sizes of these "mounds" are comparable to those of the nanodimples observed by the high-resolution SEM (Fig. 4(d, e)), it is reasonable to believe that these "mounds" detected by AFM are representative of nanodimples as well. These nanodimples have a non-uniform size distribution, since the AFM topographic image in Fig. 7c shows much smaller ones with 5 nm wide and 1 to 2 nm deep in another location of the same fracture surface.

It should be pointed out that the LME fracture surface measured by AFM had actually been exposed to low oxygen (C_O = 10^{-8} wt.%) LBE at 350 to 280°C for a few hours, since the LBE in the testing tank was not immediately drained off after the test was complete. This might cause liquid metal corrosion to the fresh fracture surface and thus raises the question whether the formation of the nanodimple-like features might be attributed to a slight corrosion process. To check this possibility, before performing the AFM topography measurement, a specimen was first fractured in liquid N_2 and then immersed into an oxygen-depleted LBE (C_O = 10^{-12} wt.%) for a simulated exposure test. This test demonstrated, at least under the resolution of AFM, that the short time and low

temperature exposure did not evidently modify the appearance of the fracture surface (Fig. 7d). The low temperature fracture surface produced in liquid nitrogen was exposed to air for a couple of hours, before it was transported to LBE for the simulated exposure test. As a result, the fracture surface might be covered by native oxides which could prevent the fracture surface from LBE wetting. However, the native oxides are not thermodynamically stable when exposed to the extremely low oxygen LBE environment and can be dissolved in short time. Thus, a good wetting condition is believed to have been obtained during the exposure test. Furthermore, the LBE in the testing tank was no longer fresh and had been used for a few years, therefore, the LBE was already saturated with Fe and Cr species which came from the inner surfaces of the testing tank and storage tank made of stainless steels and have low solubility in LBE. As a consequence, when the fatigue specimen was broken in the LBE, the fresh fracture surfaces were still exposed to the low oxygen LBE for a couple of hours, but this might not have resulted in significant selective dissolution of the main constituents of T91 steel (i.e. Fe and Cr) from the fracture surfaces into the saturated LBE. In a word, it is reasonable to believe that the observed nanodimples were formed during the LME cracking process, rather than caused by external factors such as liquid metal corrosion or aqueous acid corrosion during the LBE cleaning process as mentioned earlier. Each AFM topography measurement was repeated 3 to 6 times to get some statistics of precision.

3.3.3 EBSD examination of the microstructure along the crack walls and at the crack tips

The EBSD orientation maps in Fig. 8 present an interesting difference in the microstructure along either side of the fatigue cracks after testing in vacuum and in LBE at

350 °C. In vacuum, Fig. 8a shows that the martensitic laths close to the crack walls have been transformed into small equiaxed grains. Most of the grains have low angle grain boundaries, indicating that their formation is not a result of dynamic recrystallization. This grain refinement phenomenon also suggests that extensive plasticity was localized around the crack tip during the crack propagation in vacuum. In contrast, Fig. 8(b, c) shows that the fatigue crack in the presence of LBE propagates by cutting through the prior-austenite grain boundaries and the martensite lath boundaries (both the ND and TD color coding IPF maps show the same result), without markedly creating grain refinement at both sides of the crack. This observation implies the occurrence of LME and limited plastic deformation around the crack tip in the presence of LBE. Therefore, in addition to the fractographic observations, the information about whether the grain refinement is present near a crack can be used to identify the occurrence of LME, i.e. the absence of evident grain refinement could be a sensitive indicator of LME under low cycle fatigue.

The T91 specimen tested in LBE at 250 °C shows a similar fatigue crack propagation behavior and grain refinement is not seen beneath the fracture surface (Fig. 9). The main fatigue crack cuts through the martensite laths lying in its propagation direction to produce translath cracking, accompanied by two shallow secondary cracks propagating along the lath boundaries which are oriented at about 45° relative to the loading axis. The two cracked martensitic lath boundaries are high angle grain boundaries, which is in agreement with the result obtained by Martin et al. [52]. These two interlath decohesion cases confirm that some of the secondary cracks observed in Fig. 4b are indeed a type of interlath cracking. However, not all the lath boundaries act as a preferential LME cracking path and nearly no interlath decohesion can be observed at those boundaries oriented

parallel to the loading axis. This observation further proves that the boundary decohesion under the influence of LME is orientation dependent, and only if the orientation of the boundaries is stress-favorable (i.e. such that the stress component perpendicular to the boundary line is sufficiently high compared to the boundary strength weakened by adsorption of LBE atoms), the boundary decohesion could happen [41]. In addition, Fig. 9 shows that the fatigue crack changes its propagation direction with the variation of the crystallographic orientation of the martensite laths, leading to the formation of a "valley" on the fracture surface. This "valley" creates an illusion of a shallow secondary crack, but it should not be regarded as a crack. Probably, some of the apparent secondary cracks in Fig. 4b belong to this case. The IQ map in Fig. 9 does not show clear contrast gradients from the fracture surface to the bulk in most of the martensite laths, indicating that plasticity is limited to a very thin layer of material in close proximity to the fracture surface. However, compared to the other locations, the crystallographic orientation of the martensite lath marked with the dashed rectangle in the IPF map exhibits a much more obvious local orientation change, resulting likely from localized plastic shear deformation at that site. If so, this suggests that the plasticity at the tip of the LME crack is not homogeneous, which is in agreement with the inhomogeneous sizes of the dimples observed by the high-resolution SEM and AFM (Figs. 3c, 3d, 3e, 4e, 5c and 7).

Increasing the temperature to 400°C does not change the general effect of LME on the microstructure, see Figs. 10 and 11. The microstructure underneath the tear ridges reported in Fig. 3(a, b and c) is found to have been refined into many small grains which mostly have low angle grain boundaries (Fig. 10). This grain refinement is observed at the place where the crack propagation is drastically changed by 70° relative to the original

propagation direction. Intense plastic deformation is responsible for this grain refinement at the tear ridge with a height of 10 μm. Nevertheless, the absence of grain refinement in other places again demonstrates that the plastic deformation at the crack front in the presence of LME is not uniform.

The contrast gradient around the crack tip revealed by the IQ map in Fig. 11 suggests the presence of some lattice distortion in the vicinity of the crack tip. The crack tip seems to propagate along a lath boundary (marked with the rectangle in the IPF map), even if obvious translath cracking is visible behind the crack tip (e.g. the places marked with the double arrows). This observation indicates that even for the interlath decohesion, some plastic deformation takes place in the vicinity of the crack tip, which is in line with the presence of microdimples observed on the intergranular facets shown in Fig. 3e. It should be mentioned that the dark contrast at the crack tip could be generated by polishing artifacts. However, the polishing artifacts, such as scratches, generally exhibit straight lines along a specific direction. Obviously, this is not the case for the contrast observed at the crack tip in Fig. 11.

3.3.4 TEM observation of the deformation microstructure underneath the fracture surface

TEM bright-field images in Fig. 12 show that the martensite laths in the vicinity of the fracture surface (e.g. region A, see Fig. 12b) of T91 steel tested in vacuum have been refined into very small grains, which confirms the EBSD observation presented in Fig. 8a. These small grains are decorated with high dislocation density and the original lath boundaries are destroyed. The diffraction pattern in region A shows a continuous diffraction “ring”, indicating a polycrystalline structure. By contrast, the degree of the grain

refinement at a site relatively far from the fracture surface (e.g. region B) is lower. The initial martensite lath boundaries still can be identified at that location, although grain subdivisions and abundant dislocations are clearly visible in the laths (Fig. 12(d, e)). The intermittent diffraction "ring" is also evidence of a relatively small number of grains in region B, compared to region A under the same objective aperture. This means that during the crack propagation, along the loading direction, there is a large stress/strain gradient from the fracture surface to the bulk and plastic strain is highly localized around the crack tip.

Fig. 13 presents the microstructure close to the fracture surface of T91 tested in LBE. It can be seen that the dislocation configurations and grain microstructures underneath the fracture surface are much different from those observed in vacuum. No evident grain refinement of the martensite laths occurs in the vicinity of the fracture surface so that the initial lath structures can be clearly identified, see Fig. 13(b-f). Fig. 13(c, d) shows that the dislocation density inside most of the martensite laths is low, but relatively many dislocations do exist in a few laths, as shown in Fig. 13(e, f). Fig. 13d also shows that when the crack passes through two neighboring martensite laths with different orientations, a shallow secondary crack (20 nm deep) is created at the lath boundary nearly parallel to the loading axis. This indicates that translath cracking is accompanied by interlath decohesion, and if the lath boundary is oriented stress-unfavorably, the interlath crack is expected to be short. This observation is consistent with the interlath cracking phenomenon observed by the high resolution SEM and EBSD (Figs. 4 and 9).

The bright-field image in Fig. 14a shows two sectioned nanoscale dimples at the fracture surface and their sizes are consistent with those observed by AFM in Fig. 7. The

ACOM-TEM technique was used to measure the misorientation underneath the two dimples (Fig. 14(b, c)), showing a slight misorientation of 1 to 4°. This TEM observation provides additional evidence that nano dimples are available at part of the LME fracture surfaces.

Both the EBSD and TEM observations have shown that most of the LME cracks at the translath cracking regions tend to approximately propagate along a specific crystallographic plane, see Figs. 9, 10 and 13d. In order to determine this crystallographic plane, two DPs with different zone axes were recorded from a martensite lath which is cut through by a LME crack. After indexing these two DPs, the cracking plane can be determined by the cross product of the two vectors (marked with red lines in the DPs) which represent two lines sitting in the cracking plane to be determined. The determination method is described in Fig. 15. The result shows that the LME fracture happens at the $(\bar{1}1\bar{1})$ plane which is consistent with the habit plane of 9 to 12 wt.% Cr martensitic steels [67, 68], instead of at the {100} cleavage plane nor at the most preferable slip planes such as {110}, {211} and {321} for bcc metals. This confirms that LME of the T91/LBE system is not pure plastic shear failure, nor pure cleavage failure.

4. Discussion

Here we discuss the observed LME fracture features of T91 embrittled by LBE on the basis of some promising LME models and mechanisms proposed in the literature to evaluate their applicability for the T91/LBE system.

The adsorption induced reduction in surface energy mechanism [9] seems not to explain the observation that neither intergranular boundary cracking nor interlath decohesion is the dominant failure mode for the main fatigue crack, as evidenced in Figs. 8(b, c), 9, 10 and 11. Actually, from the thermodynamics point of view, the grain boundary energy (γ_{gb}) should provide an additional driving force for the liquid metal atoms to be adsorbed preferentially at the boundaries, so that the reduction in surface energy in the case of cracking along the grain or lath boundaries should be thermodynamically more favorable compared to that in the case of cracking in the bulk. According to Griffith and Orowan's theory (quoted in [6]), the correlation between the stress (σ_{bulk}) required for fracturing an elastoplastic solid through the bulk and the fracture energy can be represented as follows

$$\sigma_{bulk} = \sqrt{\frac{2E(\gamma_{s/l} + \gamma_p)}{\pi a}} \quad (4)$$

where E is the Young's modulus of the solid, $\gamma_{s/l}$ is the solid-liquid interfacial energy, γ_p is the dissipated energy which is converted into heat and immobile dislocations in the plastic zone, a is the half length of an elliptical crack in the solid. Considering the contribution of grain boundary energy (γ_{gb}) to the LME-induced boundary decohesion, Eq. (4) is adapted to be

$$\sigma_{gb} = \sqrt{\frac{2E(\gamma_{s/l} + \gamma_p - \gamma_{gb})}{\pi a}} \quad (5)$$

This equation indicates that the stress required for cracking the solid is lower if the crack propagates along the grain boundaries (σ_{gb}) than if the crack propagates through the bulk (σ_{bulk}). Therefore, the quantity of boundary decohesion cases for the main fatigue crack

should be more than that of translath or trangranular cracking cases. However, this is contradictory with the observations presented in this study, indicating that the grain boundary energy (γ_{gb}) may not be the dominant driving force for LME. Furthermore, the ab initio electronic structure calculations on the surface energy reduction of pure iron by adsorption of LBE species have shown that the adsorption at the $\{011\}$ plane leads to the greatest surface energy reduction (35%), followed by 22% for the $\{001\}$ plane and 16% for the $\{111\}$ plane [71]. This calculation result predicts that the preferable LME cracking plane is $\{011\}$. However, this prediction is not in accordance with the real LME cracking plane $\{\bar{1}1\bar{1}\}$, as determined in Fig. 15.

Similarly, the two grain boundary penetration models [15, 16] do not explain the observation that boundary decohesion is not the dominant failure mode for the main fatigue crack in the T91/LBE system. In addition, both models insist that the time-consuming atomic diffusion along the boundaries has a decisive effect on the crack initiation and subsequent crack propagation, which cannot account for the fast fatigue crack propagation rate of 60 to 80 μm/s, as reported in our previous work [41].

The applicability of the stress assisted dissolution-condensation model may be discounted for the T91/LBE system, since the solubility limits of Fe and Cr in LBE are extremely low [72], and thus this greatly restricts the LME crack propagation rate. Furthermore, an equation was derived from this model to calculate the crack propagation rate [17], which can be used to quantitatively evaluate its validity in explaining the LME phenomenon of the T91/LBE system, as follows

$$\frac{\mathrm{d}a}{\mathrm{d}t} = \left(\frac{C_{o,s} D \omega^2 \gamma}{kT}\right) \frac{1}{\rho^2} \left(\frac{2a\sigma_a^2}{E\gamma} - 1\right) \quad (6)$$

where $C_{o,s}$ is the equilibrium concentration of the solid metal (taking Fe as an example) in the liquid metal (at 350°C, $C_{o,\,Fe}$ = 1.02x10^{13} atoms/cm^3 in LBE [73]), D is the diffusion coefficient of Fe in LBE (D = 3.5x10^{-7} cm^2/s [74]), ω is the atomic volume of Fe (ω^2 = 2.52x10^{-46} cm^6/atom), γ is the solid-liquid interfacial energy (surface tension: $\gamma_{Fe/LBE}$ = 4 mN/cm [75]), ρ is the crack tip radius (in the presence of LME, the crack tip is very sharp [51]. Assuming ρ = 0.1 μm = 10^{-5} cm), a is the half length of the crack (assuming a = 0.15 cm), σ_a is the remote applied stress (σ_a = 380 MPa, to make the issue more tractable, it is assumed that the peak tension stress in one fatigue cycle is approximately identical with the stress at the crack tip), E is the Young's modulus (E = 190 GPa at 350°C [76]), k is the Boltzmann's constant (k = 1.3806488x10^{-23} J/K), T is the temperature in Kelvin (623 K). Inserting all the parameters above into Eq.(6) allows for an estimated velocity of the crack growth under the influence of LME: da/dt = 2.4x10^{-8} cm/s = 2.4x10^{-4} μm/s, which is far smaller than 60-80 μm/s calculated in terms of the SEM observation of the fatigue striations on the fracture surfaces [41]. Hence, this further verifies that the stress-assisted dissolution-condensation model is not suitable to account for the LME-induced fast fatigue crack propagation observed in the T91/LBE system.

Considering that the adsorption of liquid metal atoms at the crack tip can only influence a few atomic distances due to an electronic screening effect caused by a rather high concentration of mobile free electrons in the metal, therefore, the adsorption enhanced work hardening mechanism [19] may not be suitable for the T91/LBE system, since the enhanced dislocation emission occurring only inside a few atomic layers is not expected to

result in pronounced work hardening. Particularly, this mechanism does not mention the formation of the nano/micro dimples as shown in Figs. 3, 4, 7 and 14.

The presence of submicron dimples at the tear ridges and the nanodimples at the flat regions in the fracture surface of T91 steel embrittled by LBE, observed in this study using the high resolution SEM and AFM, appears to support the adsorption induced dislocation emission mechanism proposed by S.P. Lynch [8, 12-14]. In this mechanism, it is proposed that adsorption of embrittler atoms facilitates dislocation emission from the crack tip to produce fast crack advance and the cracks grow by alternate slip. The crack propagates rapidly to intersect voids formed in the plastic zone around the crack tip. It should be mentioned that according to this mechanism, one would expect a dislocation gradient from the fracture surface to the bulk, which is not observed by TEM (Fig. 13), but this may not be an argument to discount the validity of this mechanism, considering that dislocations may exist in a very small plastic zone around the crack tip [77]. This mechanism could be appropriate to explain the LME phenomenon in the T91/LBE system. Nevertheless, how to use it to interpret the non-uniform dimple sizes, as shown in Figs. 4e, 5c and 7(b, c), is not straightforward. Besides, a dislocation emission process generally leads to crack tip blunting in most crystallographic orientations, so that crack propagation should be slowed down during this process. This is also the theoretical basis of the general ductile behaviour of metallic materials. It is also not straightforward, therefore, to understand how a dislocation emission process could generate fast LME crack propagation.

So far, the adsorption induced reduction in interatomic cohesion model [10, 11] is the most widely accepted LME mechanism, since it can qualitatively account for the influence of many factors on the LME susceptibility of various solid metal/liquid metal

couples [6, 7]. However, this model generally predicts a featureless fracture surface, which somewhat contradicts the nano/micro dimples observed in the "flat" regions (Figs. 3, 4e, 7(b, c), 14a).

The evaluation of the applicability of the literature models and mechanisms for the T91/LBE system shows that some of them could well explain part of the experimental observations, for instance, the adsorption induced reduction in surface energy mechanism could account for the secondary cracking at the martensitic lath boundaries; the adsorption induced dislocation emission mechanism could interpret the formation of the nano/micro dimples; the adsorption induced reduction in interatomic cohesion model could explain why most of the fracture regions tend to be flat and "featureless". It seems, however, that none of them is able to cover all the results, i.e. the diverse LME fracture features. This implies that multiple physical processes, perhaps including the weakening-induced interatomic decohesion at the crack tip and plastic shearing in the plastic zone around the crack tip, might be involved simultaneously during the LME cracking process. The experimental results presented in this study, to some extent, support the LME mechanism proposed in our previous work [51].

In this mechanism, it was proposed that a moderate weakening effect happens to the iron atomic bond at the crack tip being intimate contact with LBE, leading to a lower tensile normal stress which is required to break the atomic bond. The moderate weakening effect reduces the shear strength of the interatomic planes at the crack tip as well. Nevertheless, this effect is only limited to a few atomic distances as mentioned earlier. It is assumed that despite of this weakening effect, the critical tensile normal stress σ_c required

to break the atomic bond is still higher than the critical resolved shear stress τ_c required to activate dislocation glide at a given slip plane. Under an external tensile force, the shear stress component along slip planes around the crack tip reaches τ_c before the tensile normal stress component reaches σ_c. Immediately after this event, plastic deformation via dislocation slip occurs and generates excess vacancies into the plastic zone. The proceeding dislocation slip releases the tensile normal stress component and the generated vacancies can coalesce into nano/micro voids as the plastic strain increases. In addition to these voids, other defects such as dislocations could accumulate in the plastic zone as well. All of these defects cause strain hardening, i.e. the dislocation mobility is decreasing. As a consequence, τ_c is gradually increasing as the plastic deformation proceeds and the shear stress component gets more and more difficult to reach the increasing τ_c. Meanwhile, the tensile normal stress cannot be released effectively and instead it increases gradually to reach σ_c after a certain moment, followed by breaking of the atomic bond. The same scenario will happen to the successive atomic bonds next to the first atomic bond at the crack tip. Finally, the LME crack intersects the hardened plastic zone as well as the nano/micro voids inside it to form the nano/micro dimples on the LME fracture surface. The size of the voids formed in the plastic zone depends mainly on the degree of the weakening effect, and partially on the orientation of the grain or grain boundaries containing the crack tip, on residual stresses in the material as well as on dislocation obstacles, etc. The variable sizes of the dimples observed in Figs. 3, 4e, and 7(b,c) might be due to the inhomogeneous microstructures and different stress states at the crack tip. The reason why the dimples in the presence of LME are small and even they sometimes are not very visible (Fig. 5c) is because LME reduces

significantly, but not completely, the crack tip plasticity. Due to the same reason, grain refinement beneath the LME fracture surface is nearly absent (Figs. 8b, 9, 10, 11 and 13) and only slight misorientation change is present underneath the nano dimples (Fig. 14).

5. Conclusions

With a combination of high resolution SEM/AFM fractography as well as EBSD/TEM examination of the deformation microstructure beneath the fracture surface of T91 steel embrittled by LBE under low cycle fatigue, the understanding of the LME-induced fracture morphology has been greatly improved. The fracture surface of T91 in the presence of LME has been shown to be characterized by three major features: quasi-brittle flat regions partially covered by nanodimples, numerous shallow secondary cracks propagating along the martensite lath boundaries and tear ridges covered by submicron dimples. The microstructure underneath the flat regions exhibits low dislocation density and slight microstructural modifications, contrary to the high dislocation density and substantial grain refinement observed in the specimens tested in vacuum. The diverse LME fracture features observed in this work could be ascribed to multiple physical processes, including the weakening-induced interatomic decohesion at the crack tip and the plastic shearing induced nano/micro voiding in the plastic zone.

Acknowledgments

The work is financially supported by the MYRRHA project, SCK•CEN, Belgium and partly funded by the European Atomic Energy Community's (Euratom) Seventh Framework Programme FP7/2007-2013 under grant agreement No. 604862 (MatISSE project) and in the framework of the EERA (European Energy Research Alliance) Joint Programme on Nuclear Materials. Dr. Tom Van der Donck (KU Leuven) is acknowledged for the EBSD measurements. The authors are grateful to Dr. Van Renterghem Wouter (SCK•CEN) for fruitful discussion of the TEM results. Xing Gong sincerely acknowledges valuable suggestions from Dr. S.P. Lynch (Defence Science and Technology Organisation and Monash University, Melbourne, Australia).

References

[1] M.H. Kamdar, Embrittlement by liquid metals, Prog. Mater Sci. 15 (1973) 289-374.

[2] C.F. Old, Liquid metal embrittlement of nuclear materials, J. Nucl. Mater. 92 (1980) 2-25.

[3] M.G. Nicholas, C.F. Old, Liquid metal embrittlement, J. Mater. Sci. 14 (1979) 1-18.

[4] R.E. Clegg, A fluid flow based model to predict liquid metal induced embrittlement crack propagation rates, Eng. Fract. Mech. 68 (2001) 1777-1790.

[5] P.J.L. Fernandes, R.E. Clegg, D.R.H. Jones, Failure by liquid metal induced embrittlement, Eng. Fail. Anal. 1 (1994) 51-63.

[6] P.J.L. Fernandes, D.R.H. Jones, Mechanisms of liquid metal induced embrittlement, Int. Mater. Rev. 42 (1997) 251-261.

[7] B. Joseph, M. Picat, F. Barbier, Liquid metal embrittlement: A state-of-the-art appraisal, Eur. Phys. J. Appl. Phys. 5 (1999) 19-31.

[8] S.P. Lynch, Mechanisms and kinetics of environmentally assisted cracking: current status, issues, and suggestions for further work, Metall. Mater. Trans. A 44 (2013) 1209-1229.

[9] W. Rostoker, J.M. McCaughey, H. Markus, Embrittlement of Liquid Metals, Reinhold Publishing Corporation, New York, 1960.

[10] A.R.C. Westwood, M.H. Kamdar, Concerning liquid metal embrittlement, particularly of zinc monocrystals by mercury, Philos. Mag. 8 (1963) 787-804.

[11] N.S. Stoloff, T.L. Johnston, Crack propagation in a liquid metal environment, Acta Metall. 11 (1963) 251-256.

[12] S.P. Lynch, Liquid-metal embrittlement in an Al 6% Zn3% Mg alloy, Acta Metall. 29 (1981) 325-340.

[13] S.P. Lynch, Environmentally assisted cracking: overview of evidence for an adsorption-induced localised-slip process, Acta Metall. 36 (1988) 2639-2661.

[14] S.P. Lynch, Metallographic contributions to understanding mechanisms of environmentally assisted cracking, Metallog. 23 (1989) 147-171.

[15] P.C. Hancock, M.B. Ives, The role of plastic deformation in liquid metal embrittlement, Can. Metall. Q. 10 (1971) 207-211.

[16] P. Gordon, H.H. An, The mechanisms of crack initiation and crack propagation in metal-induced embrittlement of metals, Metall. Trans. A 13 (1982) 457-472.

[17] W.M. Robertson, Propagation of a crack filled with liquid metal, Trans. Met. Soc. AIME 236 (1966) 1478-1482.

[18] E.E. Glickman, Dissolution Condensation Mechanism of Stress Corrosion Cracking in Liquid Metals: Driving Force and Crack Kinetics, Metall. Mater. Trans. A 42 (2011) 250-266.

[19] I.G. Dmukhovskaya, V.V. Popovich, A phenomenological model of embrittlement of metals under conditions of the adsorption action of liquid metal media, Mater. Sci. 18 (1983) 461-467.

[20] S. Guerin, J.L. Pastol, C. Leroux, D. Gorse, Synergy effect of LBE and hydrogenated helium on resistance to LME of T91 steel grade, J. Nucl. Mater. 318 (2003) 339-347.

[21] J. Van den Bosch, D. Sapundjiev, A. Almazouzi, Effects of temperature and strain rate on the mechanical properties of T91 material tested in liquid lead bismuth eutectic, J. Nucl. Mater. 356 (2006) 237-246.

[22] Y. Dai, B. Long, F. Groeschel, Slow strain rate tensile tests on T91 in static lead-bismuth eutectic, J. Nucl. Mater. 356 (2006) 222-228.

[23] J. Van den Bosch, R.W. Bosch, D. Sapundjiev, A. Almazouzi, Liquid metal embrittlement susceptibility of ferritic-martensitic steel in liquid lead alloys, J. Nucl. Mater. 376 (2008) 322-329.

[24] Z. Hamouche-Hadjem, T. Auger, I. Guillot, D. Gorse, Susceptibility to LME of 316L and T91 steels by LBE: Effect of strain rate, J. Nucl. Mater. 376 (2008) 317-321.

[25] B. Long, Y. Dai, N. Baluc, Investigation of liquid LBE embrittlement effects on irradiated ferritic/martensitic steels by slow-strain-rate tensile tests, J. Nucl. Mater. 431 (2012) 85-90.

[26] B. Long, Y. Dai, Investigation of LBE embrittlement effects on the fracture properties of T91, J. Nucl. Mater. 376 (2008) 341-345.

[27] I. Serre, J.B. Vogt, Heat treatment effect of T91 martensitic steel on liquid metal embrittlement, J. Nucl. Mater. 376 (2008) 330-335.

[28] I. P. Serre, I. Diop, N. David, M. Vilasi, J.B. Vogt, Mechanical behavior of coated T91 steel in contact with lead–bismuth liquid alloy at 300° C, Surf. Coat. Technol. 205 (2011) 4521-4527.

[29] C.Q. Ye, J.B. Vogt, I.P. Serre, Liquid metal embrittlement of the T91 steel in lead bismuth eutectic: The role of loading rate and of the oxygen content in the liquid metal, Mater. Sci. Eng. A 608 (2014) 242-248.

[30] J. Van den Bosch, G. Coen, A. Almazouzi, J. Degrieck, Fracture toughness assessment of ferritic-martensitic steel in liquid lead–bismuth eutectic, J. Nucl. Mater. 385 (2009) 250-257.

[31] G. Coen, J. Van den Bosch, A. Almazouzi, J. Degrieck, Investigation of the effect of lead-bismuth eutectic on the fracture properties of T91 and 316L, J. Nucl. Mater. 398 (2010) 122-128.

[32] T. Auger, D. Gorse, Z. Hamouche-Hadjem, J. Van den Bosch, G. Coen, A. Almazouzi, A. Hojna, K. Dalikova, F. Di Gabriele, M. Serrano, A. Gessi, P. Agostini, J.-B. Vogt, I. Serre, Fracture mechanics behavior of the T91 martensitic steel in contact with liquid lead-bismuth eutectic for application in an accelerator driven system, J. Nucl. Mater. 415 (2011) 293-301.

[33] Z. Hadjem-Hamouche, T. Auger, I. Guillot, Temperature effect in the maximum propagation rate of a liquid metal filled crack: The T91 martensitic steel/Lead-Bismuth Eutectic system, Corros. Sci. 51 (2009) 2580-2587.

[34] A. Hojna, F. Di Gabriele, On the kinetics of LME for the ferritic–martensitic steel T91 immersed in liquid PbBi eutectic, J. Nucl. Mater. 413 (2011) 21-29.

[35] J.-B. Vogt, A. Verleene, I. Serre, A. Legris, Mechanical behaviour of the T91 martensitic steel under monotonic and cyclic loadings in liquid metals, J. Nucl. Mater. 335 (2004) 222-226.

[36] A. Verleene, J.-B. Vogt, I. Serre, A. Legris, Low cycle fatigue behaviour of T91 martensitic steel at 300°C in air and in liquid lead bismuth eutectic, Int. J. Fatigue, 28 (2006) 843-851.

[37] J.-B. Vogt, I. Proriol-Serre, Fatigue Behaviour of a Martensitic and an Austenitic Steel in Heavy Liquid Metals, Procedia Eng. 55 (2013) 812-818.

[38] A. Weisenburger, A. Heinzel, C. Fazio, G. Müller, V.G. Markow, A.D. Kastanov, Low cycle fatigue tests of surface modified T91 steel in 10^{-6} wt% oxygen containing $Pb_{45}Bi_{55}$ at 550°C, J. Nucl. Mater. 377 (2008) 261-267.

[39] D. Kalkhof, M. Grosse, Influence of PbBi environment on the low-cycle fatigue behavior of SNS target container materials, J. Nucl. Mater. 318 (2003) 143-150.

[40] D. Gorse, T. Auger, J.-B. Vogt, I. Serre, A. Weisenburger, A. Gessi, P. Agostini, C. Fazio, A. Hojna, F.Di. Gabriele, J. Van Den Bosch, G. Coen, A. Almazouzi, M. Serrano, Influence of liquid lead and lead-bismuth eutectic on tensile, fatigue and creep properties of ferritic/martensitic and austenitic steels for transmutation systems, J. Nucl. Mater. 415 (2011) 284-292.

[41] X. Gong, P. Marmy, L. Qin, B. Verlinden, M. Wevers, M. Seefeldt, Effect of liquid metal embrittlement on low cycle fatigue properties and fatigue crack propagation behavior of a modified 9Cr-1Mo ferritic-martensitic steel in an oxygen-controlled lead-bismuth eutectic environment at 350° C, Mater. Sci. Eng. A 618 (2014) 406-415.

[42] H.A. Abderrahim, Multi-purpose hYbrid Research Reactor for High-tech Applications a multipurpose fast spectrum research reactor, Int. J. Energy Res. 36 (2012) 1331-1337.

[43] B. Long, Z. Tong, F. Gröschel, Y. Dai, Liquid Pb-Bi embrittlement effects on the T91 steel after different heat treatments, J. Nucl. Mater. 377 (2008) 219-224.

[44] F. Di Gabriele, A. Doubková, A. Hojná, Investigation of the sensitivity to EAC of steel T91 in contact with liquid LBE, J. Nucl. Mater. 376 (2008) 307-311.

[45] J.-B. Vogt, A. Verleene, I. Serre, F. Balbaud-Célérier, A. Terlain, Coupling effects between corrosion and fatigue in liquid Pb-Bi of T91 martensitic steel. Proc. Eurocorr2005, Lisbonne, 2005.

[46] T. Auger, G. Lorang, S. Guérin, J.L. Pastol, D. Gorse, Effect of contact conditions on embrittlement of T91 steel by lead-bismuth. J. Nucl. Mater. 335 (2004) 227-231.

[47] S. Gavrilov, M. Lambrecht, G. Coen, E. Stergar, J. Van den Bosch, PIE of ASTIR: Report on the full set of results of tests on irradiated and non-irradiated specimens, in FP7-212175-GETMAT. 2014, SCK·CEN: Mol, Belgium.

[48] L. Martinelli, F. Balbaud-Célérier, A. Terlain, S. Delpech, G. Santarini, J. Favergeon, G. Moulin, M. Tabarant, G. Picard, Oxidation mechanism of a Fe-9Cr-1Mo steel by liquid Pb-Bi eutectic alloy (Part I), Corros. Sci. 50 (2008) 2523-2536.

[49] L. Martinelli, F. Balbaud-Célérier, A. Terlain, S. Bosonnet, G. Picard, G. Santarini, Oxidation mechanism of an Fe-9Cr-1Mo steel by liquid Pb-Bi eutectic alloy at 470°C (Part II), Corros. Sci. 50 (2008) 2537-2548.

[50] L. Martinelli, F. Balbaud-Célérier, G. Picard, G. Santarini, Oxidation mechanism of a Fe-9Cr-1Mo steel by liquid Pb-Bi eutectic alloy (Part III), Corros. Sci. 50 (2008) 2549-2559.

[51] X. Gong, P. Marmy, B. Verlinden, M. Wevers, M. Seefeldt, Low cycle fatigue behavior of a modified 9Cr-1Mo ferritic-martensitic steel in lead-bismuth eutectic at 350°C - Effects of oxygen concentration in the liquid metal and strain rate, Corros. Sci. 94 (2015) 377-391.

[52] M.L. Martin, T. Auger, D.D. Johnson, I.M. Robertson, Liquid-metal-induced fracture mode of martensitic T91 steels, J. Nucl. Mater. 426 (2012) 71-77.

[53] S. Hémery, T. Auger, J.L. Courouau, F. Balbaud-Célérier, Effect of oxygen on liquid sodium embrittlement of T91 martensitic steel, Corros. Sci. 76 (2013) 441-452.

[54] S. Hémery, T. Auger, J.L. Courouau, F. Balbaud-Célérier, Liquid metal embrittlement of an austenitic stainless steel in liquid sodium, Corros. Sci. 83 (2014) 1-5.

[55] W. Ludwig, E. Pereiro-López, D. Bellet, In situ investigation of liquid Ga penetration in Al bicrystal grain boundaries: grain boundary wetting or liquid metal embrittlement? Acta Mater. 53 (2005) 151-162.

[56] W. Sigle, G. Richter, M. Rühle, S. Schmidt, Insight into the atomic-scale mechanism of liquid metal embrittlement, Appl. Phys. Lett. 89 (2006) 121911.

[57] M. Rajagopalan, M.A. Bhatia, M.A. Tschopp, D.J. Srolovitz, K.N. Solanki, Atomic-scale analysis of liquid-gallium embrittlement of aluminum grain boundaries, Acta Mater. 73 (2014) 312-325.

[58] E. Senel, J.C. Walmsley, S. Diplas, K. Nisancioglu, Liquid metal embrittlement of aluminium by segregation of trace element gallium, Corros. Sci. 85 (2014) 167-173.

[59] J. Luo, H. Cheng, K.M. Asl, C.J. Kiely, M.P. Harmer, The role of a bilayer interfacial phase on liquid metal embrittlement, Science 333 (2011) 1730-1733.

[60] K.M. Asl, J. Luo, Impurity effects on the intergranular liquid bismuth penetration in polycrystalline nickel, Acta Mater. 60 (2012) 149-165.

[61] K. Wolski, V. Laporte, Grain boundary diffusion and wetting in the analysis of intergranular penetration, Mater. Sci. Eng. A 495 (2008) 138-146.

[62] K.D. Bauer, M. Todorova, K. Hingerl, J. Neugebauer, A first principles investigation of zinc induced embrittlement at grain boundaries in bcc iron, Acta Mater. 90 (2015) 69-76.

[63] P. Marmy, X. Gong, LIMETS 3, a novel system for high strain fatigue testing in lead-bismuth eutectic, J. Nucl. Mater. 450 (2014) 256-261.

[64] X. Gong, P. Marmy, L. Qin, B. Verlinden, M. Wevers, M. Seefeldt, Temperature dependence of liquid metal embrittlement susceptibility of a modified 9Cr-1Mo steel under low cycle fatigue in lead-bismuth eutectic at 160 to 450°C, J. Nucl. Mater. 2015, doi:10.1016/j.jnucmat.2015.06.021.

[65] J. Lim, A. Marien, K. Rosseel, A. Aerts, J. Van den Bosch, Accuracy of potentiometric oxygen sensors with Bi/Bi_2O_3 reference electrode for use in liquid LBE, J. Nucl. Mater. 429 (2012) 270-275.

[66] G. Manfredi, J. Lim, K. Rosseel, A. Aerts, Th Doneux, C. Buess-Herman, J. Van den Bosch, Comparison of solid metal-metal oxide reference electrodes for potentiometric oxygen sensors in liquid lead-bismuth eutectic operating at low temperature ranges, Sens. Actuators B: Chem. 214 (2015) 20-28.

[67] B. Fournier, M. Sauzay, F. Barcelo, E. Rauch, A. Renault, T. Cozzika, L. Dupuy, A. Pineau, Creep-Fatigue Interactions in a 9 Pct Cr-1 Pct Mo Martensitic Steel: Part II. Microstructural Evolutions, Metall. Mater. Trans. A 40 (2009) 330-341.

[68] H. Kitahara, R. Ueji, N. Tsuji, Y. Minamino, Crystallographic features of lath martensite in low-carbon steel, Acta Mater. 54 (2006) 1279-1288.

[69] T. Neeraj, R. Srinivasan, J. Li, Hydrogen embrittlement of ferritic steels: Observations on deformation microstructure, nanoscale dimples and failure by nanovoiding, Acta Mater. 60 (2012) 5160-5171.

[70] M.L. Martin, I.M. Robertson, P. Sofronis, Interpreting hydrogen-induced fracture surfaces in terms of deformation processes: A new approach, Acta Mater. 59 (2011) 3680-3687.

[71] A. Legris, G. Nicaise, J.-B. Vogt, J. Foct, Liquid metal embrittlement of the martensitic steel 91: influence of the chemical composition of the liquid metal: Experiments and electronic structure calculations, J. Nucl. Mater. 301 (2002) 70-76.

[72] S. Gossé, Thermodynamic assessment of solubility and activity of iron, chromium, and nickel in lead bismuth eutectic, J. Nucl. Mater. 449 (2014) 122-131.

[73] C. Schroer, J. Konys, Physical chemistry of corrosion and oxygen control in liquid lead and lead-bismuth eutectic, in FZK reports. 2007, FZK: Karlsruhe, Germany.

[74] Handbook on Lead-bismuth Eutectic Alloy and Lead Properties, Materials Compatibility, Thermal-hydraulics and Technologies, OECD/NEA Nuclear Science Committee, 2007.

[75] E. Ricci, R. Novakovic, D. Giuranno, F. Gnecco, Thermo-physical data of lead-bismuth liquid alloys, TECLA internal report No.FIKW-CT-2000-00092, National Research Council (CNR), Italy, 2003.

[76] E. Stergar, M. Lambrecht, S. Gavrilov, K. Lambrinou, P. Marmy, F. Ersoy, X. Gong, MYRRHA Materials Assessment Report, 2011, SCK•CEN, Mol, Belgium.

[77] S.P. Lynch, Interpreting hydrogen-induced fracture surfaces in terms of deformation processes: A new approach, Scr. Mater. 65 (2011) 851-854.

Figure captions

Fig. 1. Microstructure of as-received T91 steel: (a) Optical micrograph; (b) EBSD orientation map; (c) Distribution of misorientation angle of martensitic laths; (d, e) TEM bright-field images; (f) Schematic illustration of the main microstructure.

Fig. 2. Strain-life diagram of T91 steel in LBE and in vacuum at 250, 350 and 450°C. The oxygen concentration in LBE is in the range of 1.28×10^{-7} to 5.46×10^{-11} wt.%. The strain rate is about 4.5×10^{-3} s^{-1}. Part of the data has been published in Refs. [51, 64].

Fig. 3. SEM fractographic micrographs show a typical quasi-brittle fracture surface after testing in LBE, covered by many tear ridges (a) on which submicron dimples are present (b, c); Large dimples with a size of 15 μm can be observed as well (d); Microdimples are present on the intergranular facets (e). The T91 specimen in (a to d) was tested under the conditions: T = 350°C, ε_a = 0.76%, C_O = 5.8×10^{-9} wt.%; The T91 specimen in (e) was tested at 160°C, ε_a = 0.43%, C_O = 3.80×10^{-9} wt.%.

Fig. 4. High resolution SEM fractographic micrographs showing very rough fracture surface after testing in LBE, characterized by numerous tiny secondary cracks and flat "featureless" regions (a, b); The tiny secondary cracks seem to propagate along the martensite lath boundaries (b, c); The flat regions are not perfectly featureless but are covered by a large number of nanoscale dimples with a size of 30 nm (d, e). The arrows indicate the positions of the secondary cracks. The T91 specimen in (a) was tested under the conditions: T = 350°C, ε_a = 0.59%, C_O = 2.88×10^{-8} wt.%; The T91 specimen in (b-e) was tested under the conditions: T = 350°C, ε_a = 0.76%, C_O = 5.8×10^{-9} wt.%.

Fig. 5. High resolution SEM fractographic micrographs of the LME fracture surface showing that the flat regions do not have as evident nanoscale dimples as those shown in Fig. 4e. The SEM pictures were taken under a tilt angle to show the relative position of two adjacent flat regions, as indicated by the two arrows (a). More details at the flat regions are shown in (b, c). The T91 specimen was tested under the conditions: T = 350°C, ε_a = 0.76%, $C_O = 5.8x10^{-9}$ wt.%.

Fig. 6. High resolution SEM micrographs of a cleavage fracture surface of T91 steel, generated by fracturing in liquid nitrogen, showing river patterns and brittle facets (a) and the absent nanoscale dimples (b).

Fig. 7. AFM topographic images of fracture surfaces: (a) fracture surface created in liquid N_2; (b, c) fatigue fracture surfaces generated in the presence of LBE under the following conditions: T = 350°C, ε_a = 0.74%, $C_O = 6x10^{-10}$ wt.%; (d) the fracture surface created in liquid N_2 and then exposed to LBE at 350 to 280°C for about 4 h.

Fig. 8. EBSD orientation maps of the microstructures along the fatigue crack walls after testing in vacuum and in LBE: (a) In vacuum: extensive grain refinement occurs at the regions close to the crack walls and most of the refined grains have low angle grain boundaries. T = 350°C, ε_a = 0.9%: (b, c) In LBE: the crack propagates mainly by cutting through the prior-austenite grain boundaries and the martensite lath boundaries without inducing grain refinement. T = 350°C, ε_a = 0.32%.

Fig. 9. EBSD orientation map (IPF) and image quality map (IQ) displaying the microstructure beneath the fracture surface after testing in LBE. No evident grain refinement can be observed. The LME crack propagates primarily in a translath way,

accompanied by a limited number of shallow interlath decohesion cases. The cracked lath boundaries are high angle grain boundaries. The T91 specimen was tested under the conditions: T = 250°C, ε_a = 0.41%.

Fig. 10. EBSD orientation map (IPF) showing that grain refinement takes place beneath a tear ridge and most of the refined small grains have low angle grain boundaries. The T91 specimen was tested under the conditions: T = 400°C, ε_a = 0.44%, LBE.

Fig. 11. EBSD orientation map (IPF) and image quality (IQ) map showing that the LME crack propagates through most of the martensite laths (translath failure mode, see the places marked with the double arrows) without inducing significant microstructural changes. The crack tip indicated with the rectangle in the IPF map showing occurrence of intergranular cracking. In the IQ map, contrast gradients seem to be present at the crack tip (see the place marked with a dashed circle), suggesting slight lattice distortion. The T91 specimen was tested under the conditions: T = 400°C, ε_a = 0.44%, LBE.

Fig. 12. Deformation microstructure beneath the fracture surface of T91 steel tested in vacuum at 350°C under ε_a = 0.9%: (a) A TEM thin foil prepared by the FIB lift-out technique; (b) The grain size close to the fracture surface is smaller than that relatively far from the fracture surface; (c) The martensite laths adjacent to the fracture surface (the distance is 100 to 200 nm) are transformed into very fine grains decorated with high dislocation density inside; (d) The profile of the martensite laths at the place about 2 μm far from the fracture surface seems not to be destroyed, but grain subdivisions and numerous dislocations are clearly visible inside them (e).

Fig. 13. Deformation microstructure beneath the fracture surface of T91 steel tested in low oxygen LBE at 350°C under ε_a = 0.76%: (a) A TEM thin foil prepared by the FIB lift-out technique; (b) No obvious grain refinement can be observed, manifested by the absence of diffraction rings (inset); (c, d) Dislocations in most of the martensite laths close to the fracture surface are not as dense as those shown in Fig. 12; (e, f) A few martensite laths contain relatively high dislocation density.

Fig. 14. TEM bright-field image showing that two sectioned nano dimples are present at the fracture surface (a); orientation mapping around the two nano dimples (b); misorientation variations underneath the two nano dimples (c). The T91 specimen was tested in LBE under the conditions: T = 350°C, ε_a = 0.76%, C_O = 5.8x10^{-9} wt.%.

Fig. 15. Determination of the crystallographic plane of the LME crack.

Fig. 1

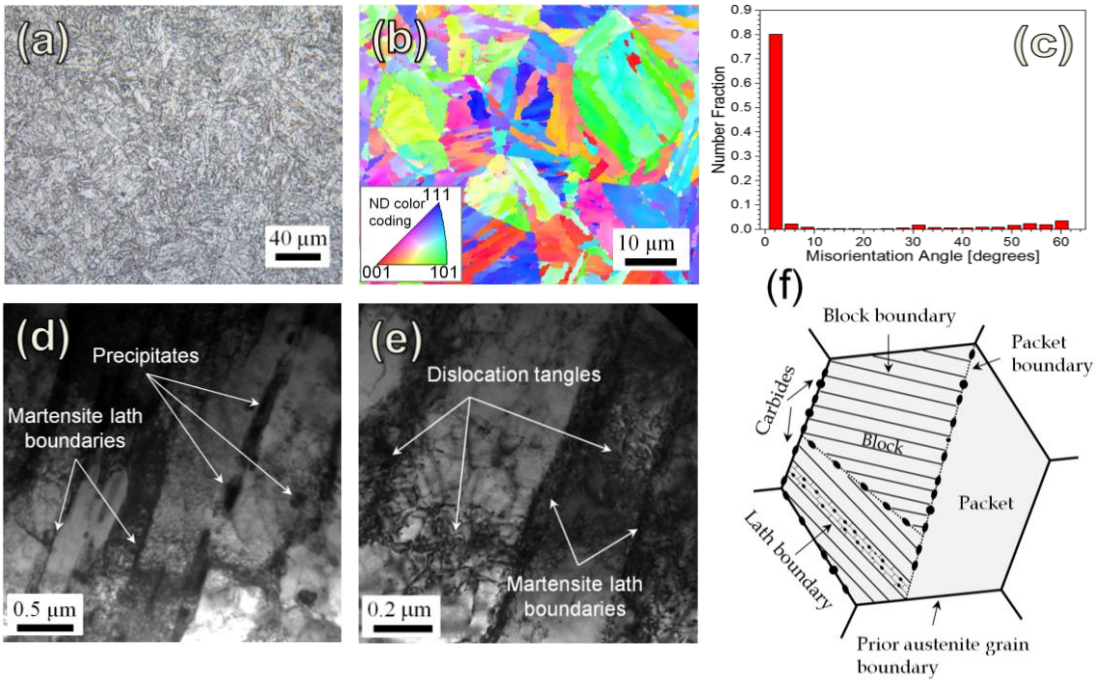
(a)
40 µm
(b)
ND color coding
111
001
101
10 µm
(c)
Number Fraction
Misorientation Angle [degrees]
(d)
Precipitates
Martensite lath boundaries
0.5 µm
(e)
Dislocation tangles
Martensite lath boundaries
0.2 µm
(f)
Block boundary
Packet boundary
Carbides
Block
Packet
Lath boundary
Prior austenite grain boundary

Fig. 2

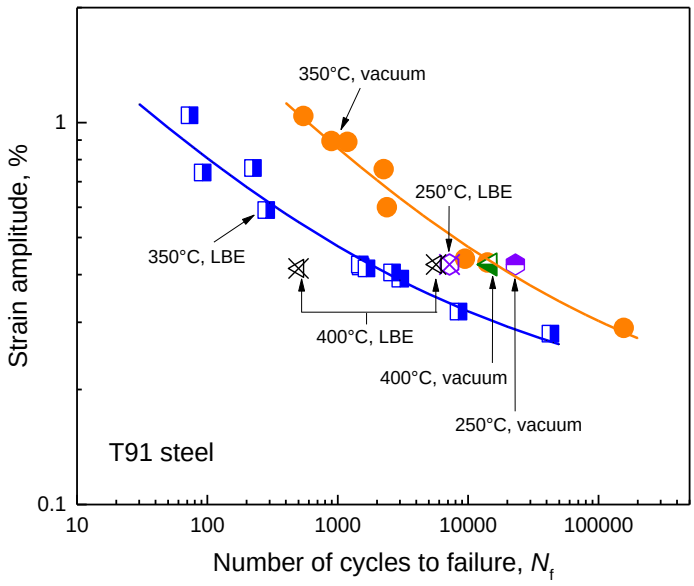
350°C, vacuum
250°C, LBE
350°C, LBE
400°C, LBE
400°C, vacuum
250°C, vacuum
T91 steel
Strain amplitude, %
1
0.1
10
100
1000
10000
100000
Number of cycles to failure, N_f

Fig. 3

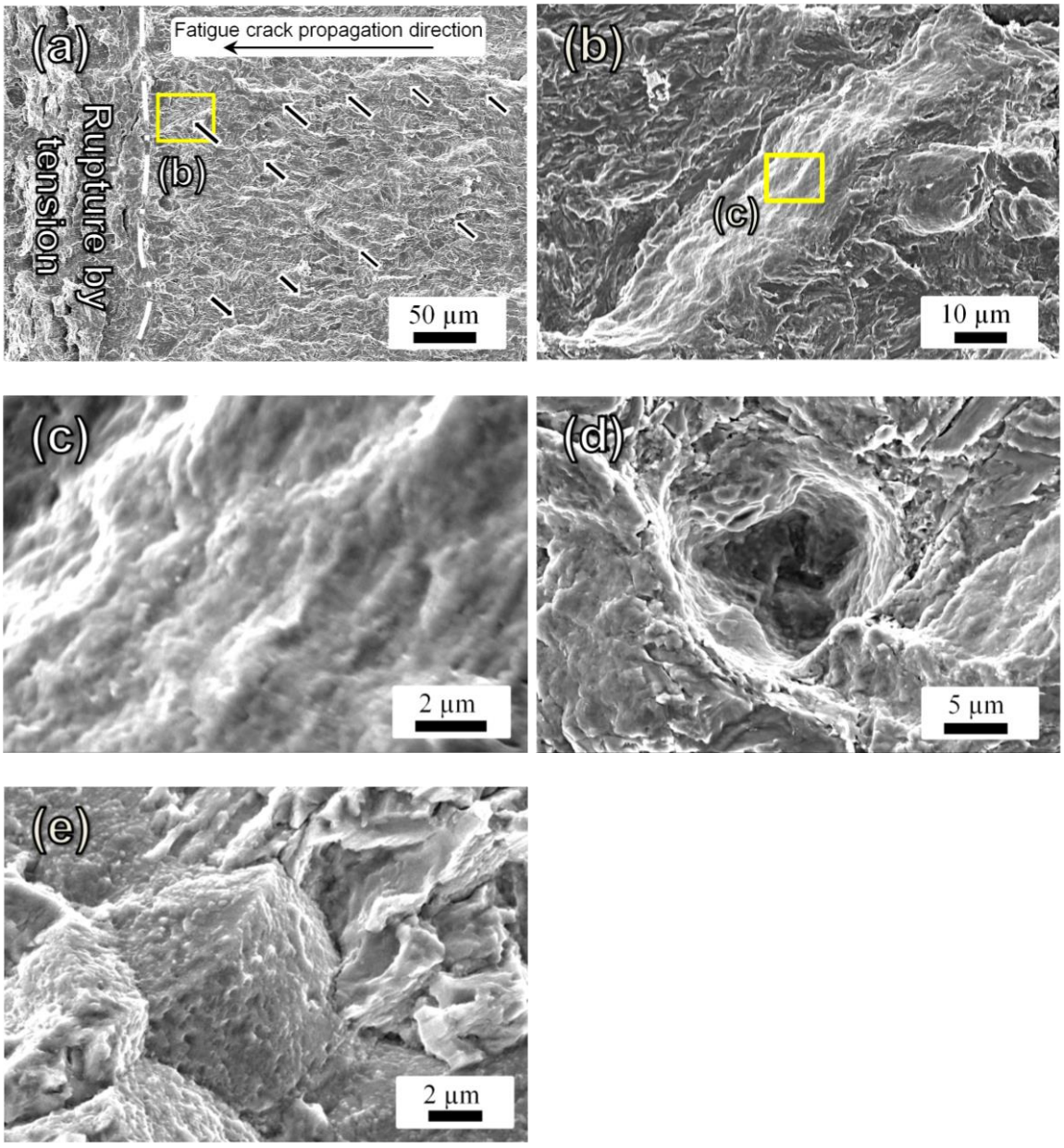
(a)
Fatigue crack propagation direction
Rupture by tension
(b)
50 µm
(b)
(c)
10 µm
(c)
2 µm
(d)
5 µm
(e)
2 µm

Fig. 4

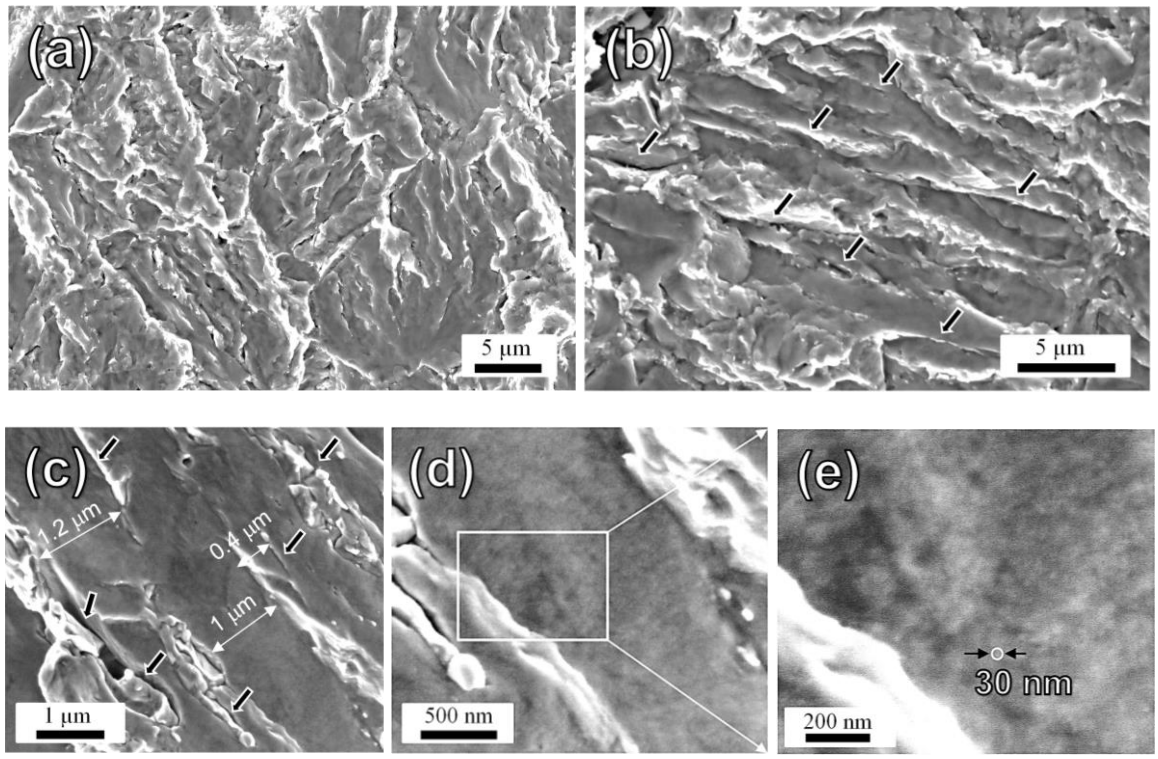

Fig. 5

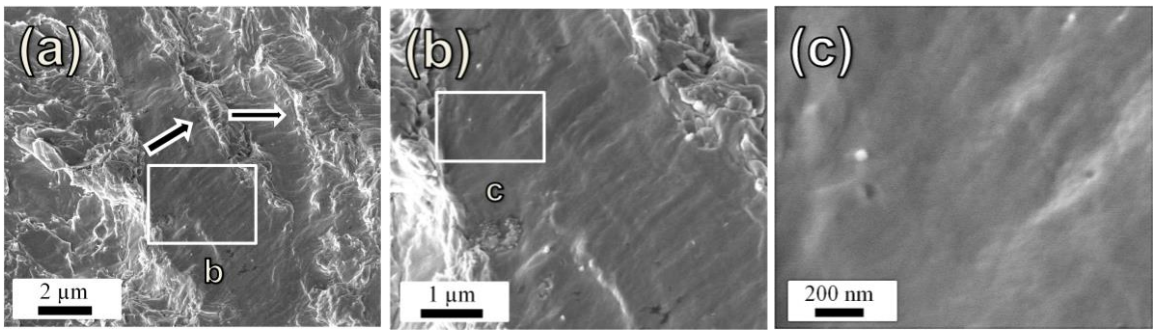

Fig. 6

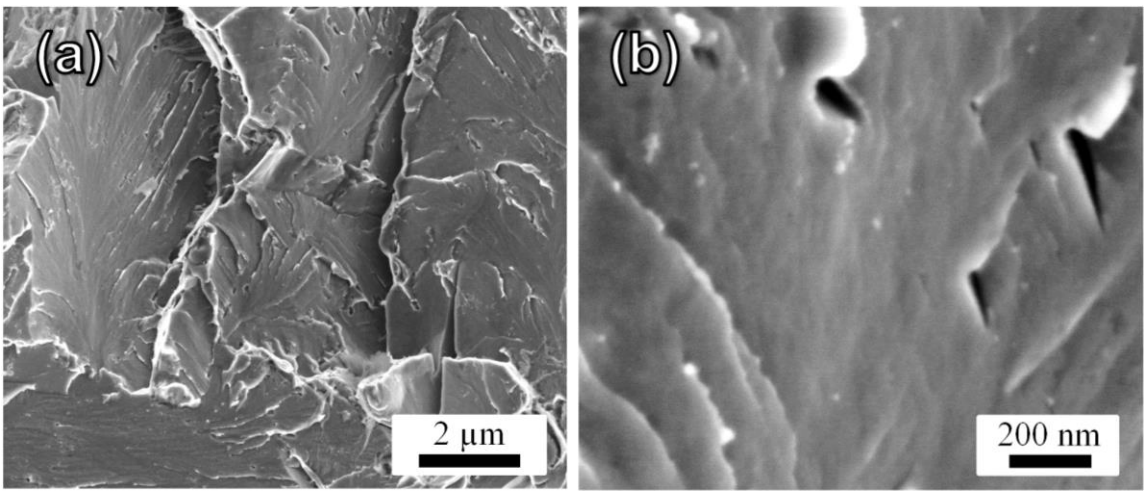

Fig. 7

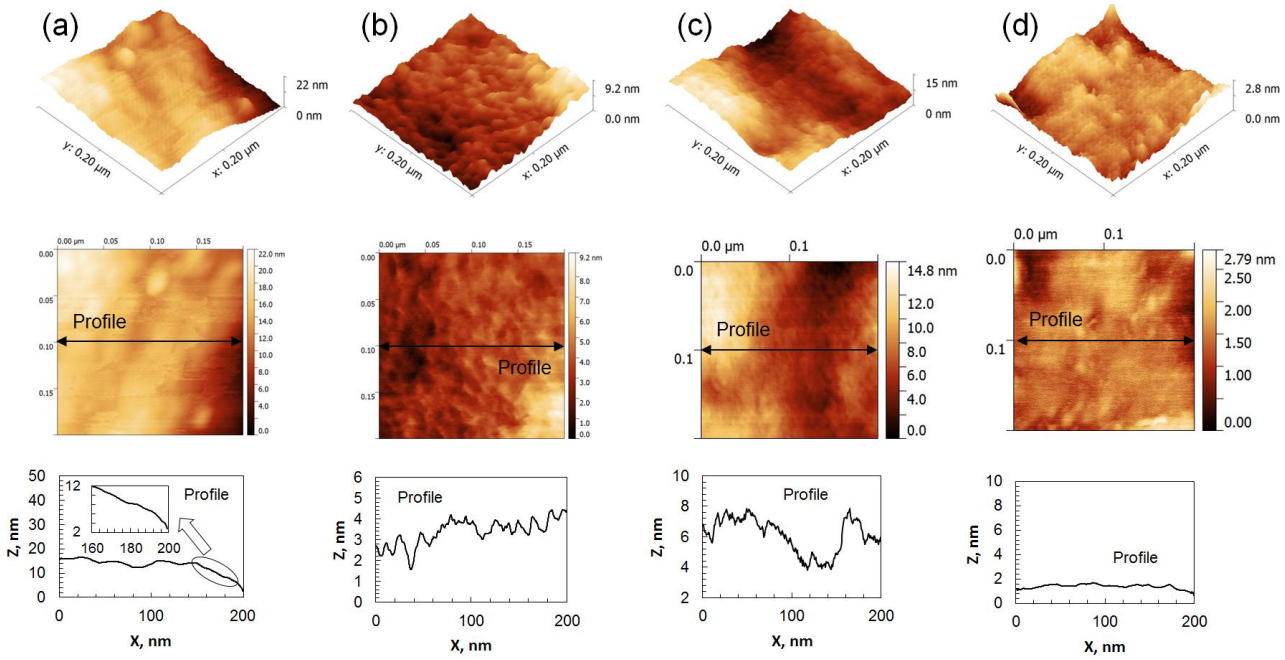
(a)
(b)
(c)
(d)
22 nm
0 nm
9.2 nm
0.0 nm
15 nm
0 nm
2.8 nm
0.0 nm
y: 0.20 µm
x: 0.20 µm
Profile
14.8 nm
2.79 nm
Z, nm
X, nm

Fig. 8

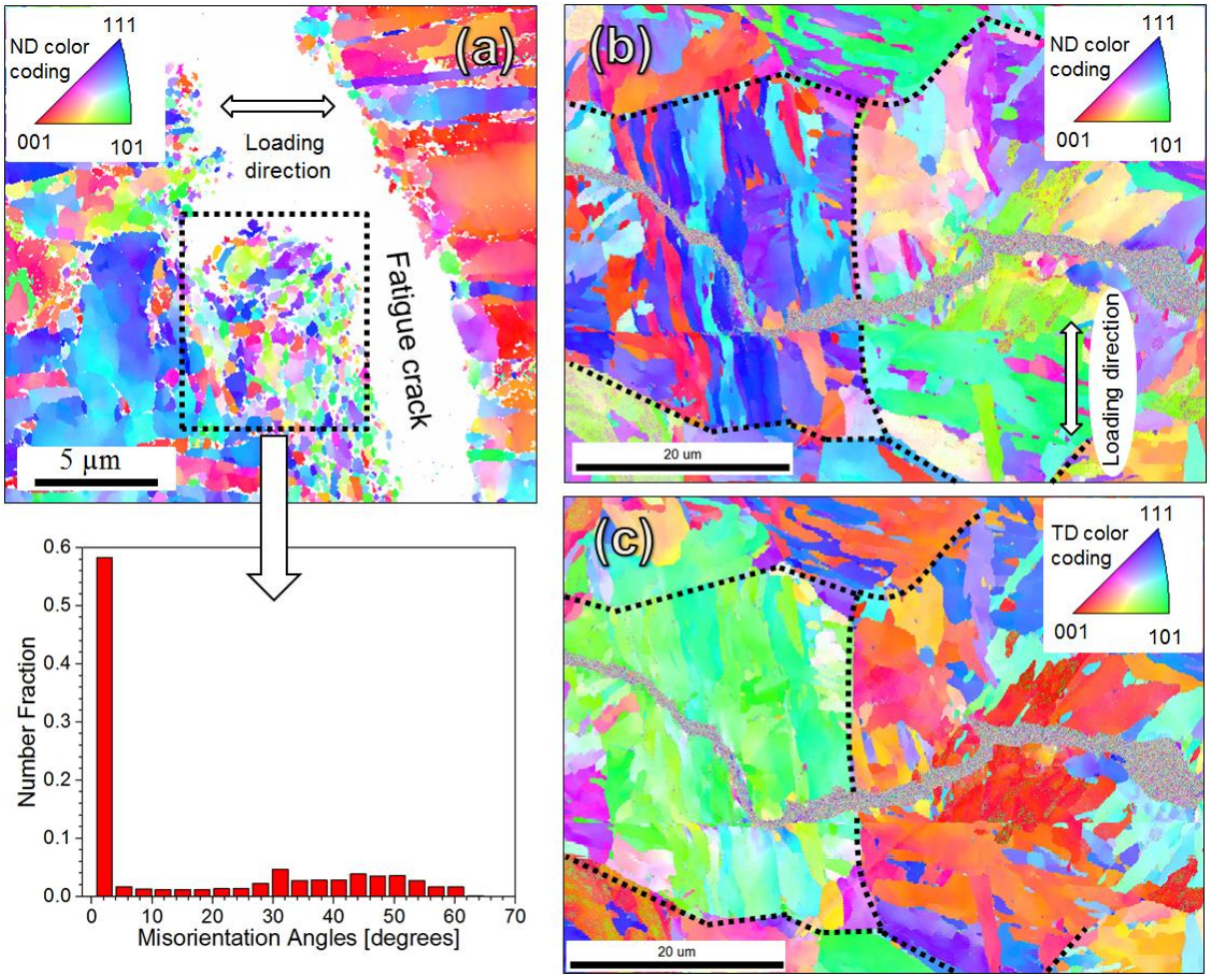
(a)
ND color coding
111
001
101
Loading direction
Fatigue crack
5 µm
Number Fraction
Misorientation Angles [degrees]
(b)
ND color coding
111
001
101
Loading direction
20 um
(c)
TD color coding
111
001
101
20 um

Fig. 9

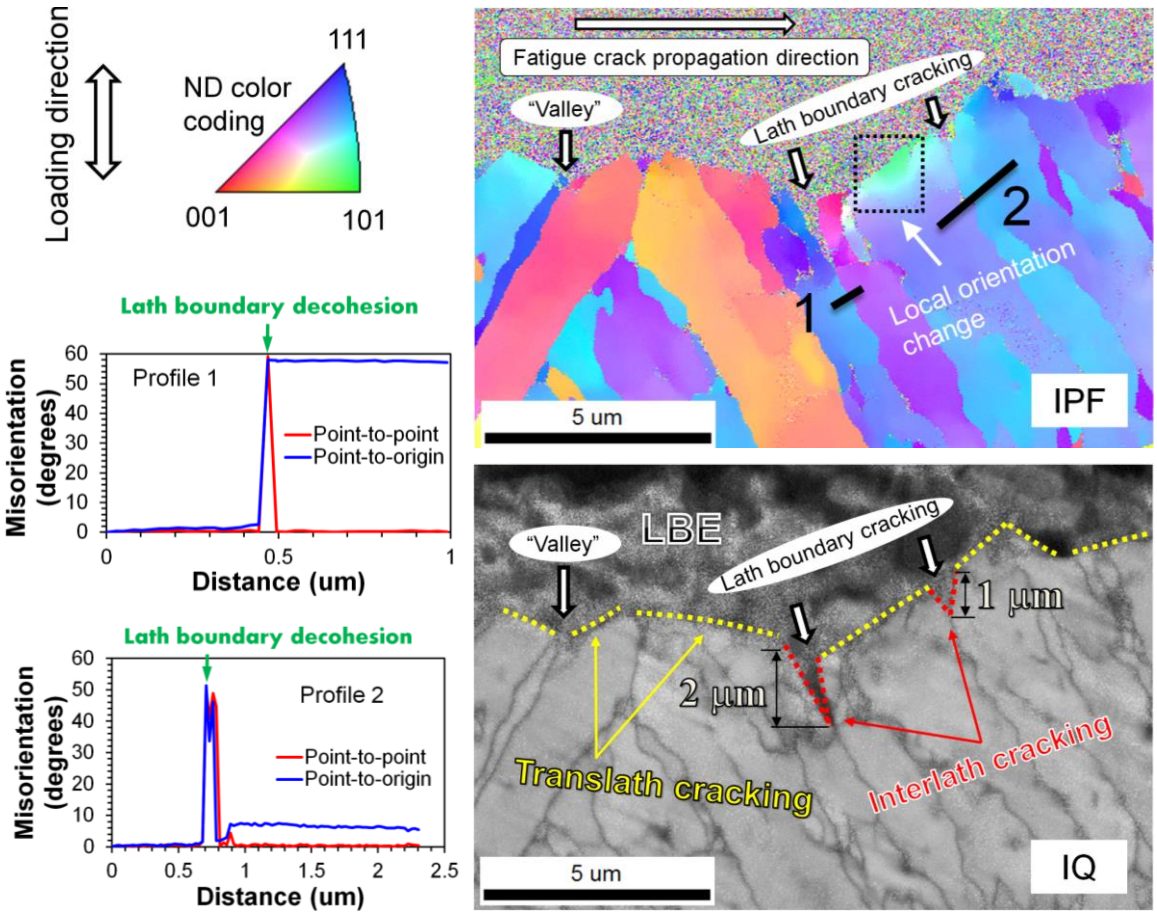
Loading direction
ND color coding
111
001
101
Lath boundary decohesion
Profile 1
Misorientation (degrees)
Distance (um)
Point-to-point
Point-to-origin
Lath boundary decohesion
Profile 2
Misorientation (degrees)
Distance (um)
Point-to-point
Point-to-origin
Fatigue crack propagation direction
"Valley"
Lath boundary cracking
1
2
Local orientation change
5 um
IPF
"Valley"
LBE
Lath boundary cracking
1 μm
2 μm
Translath cracking
Interlath cracking
5 um
IQ

Fig . 10

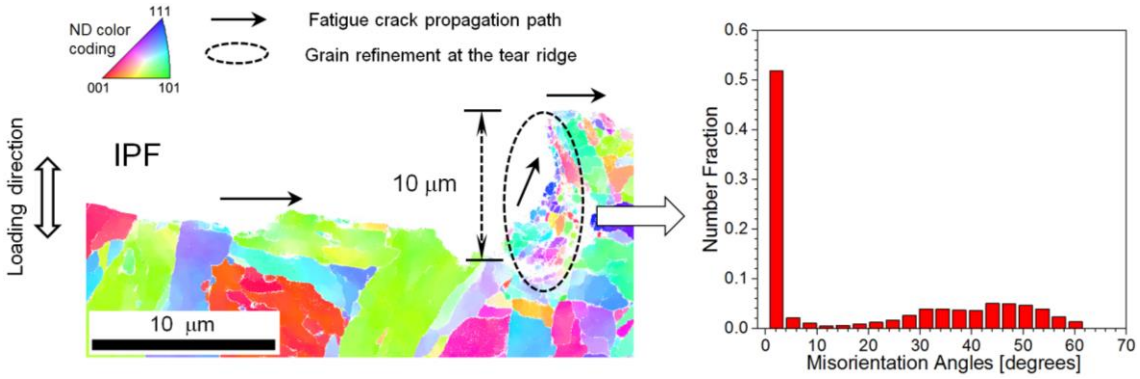
111
ND color coding
001
101
Fatigue crack propagation path
Grain refinement at the tear ridge
Loading direction
IPF
10 μm
10 μm
Number Fraction
0.0
0.1
0.2
0.3
0.4
0.5
0.6
0
10
20
30
40
50
60
70
Misorientation Angles [degrees]

Fig. 11

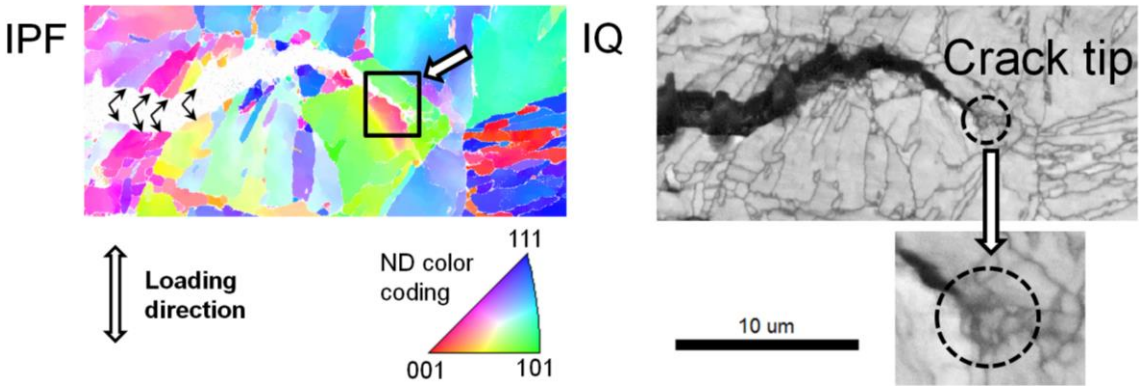
IPF
IQ
Crack tip
Loading direction
ND color coding
111
001
101
10 um

Fig. 12

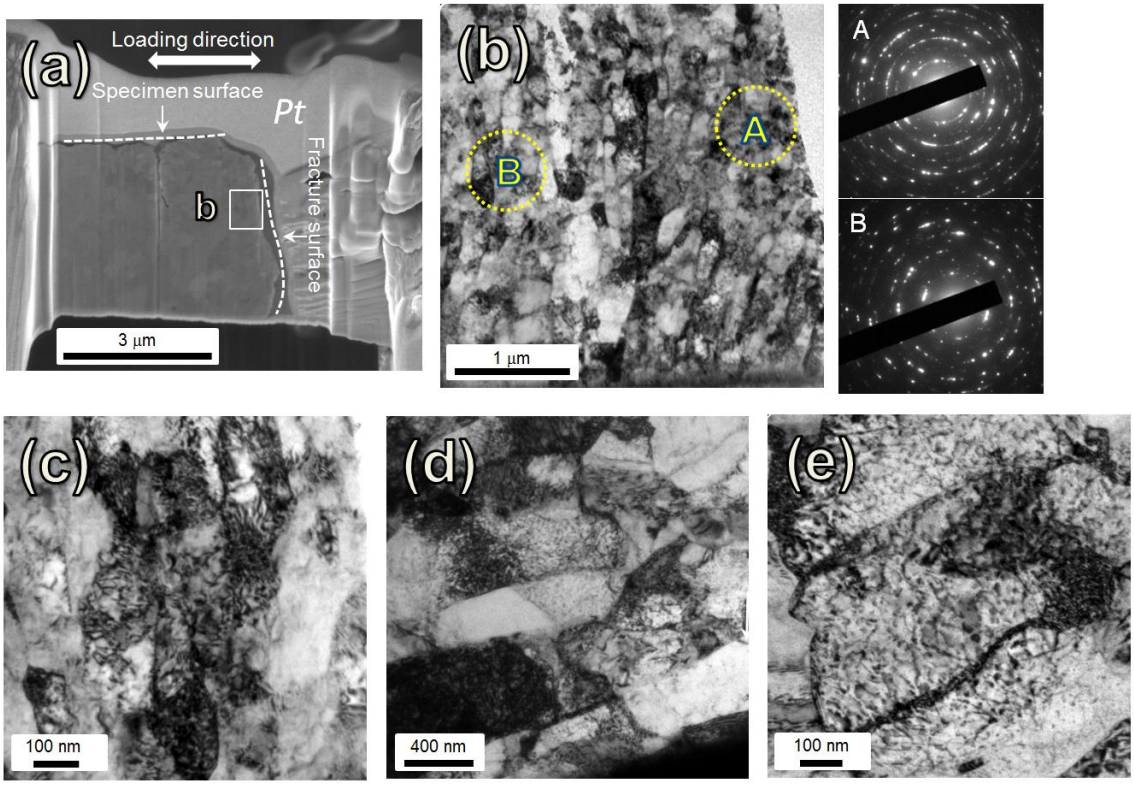
(a)
Loading direction
Specimen surface
Pt
Fracture surface
b
3 μm
(b)
A
B
1 μm
A
B
(c)
100 nm
(d)
400 nm
(e)
100 nm

Fig. 13

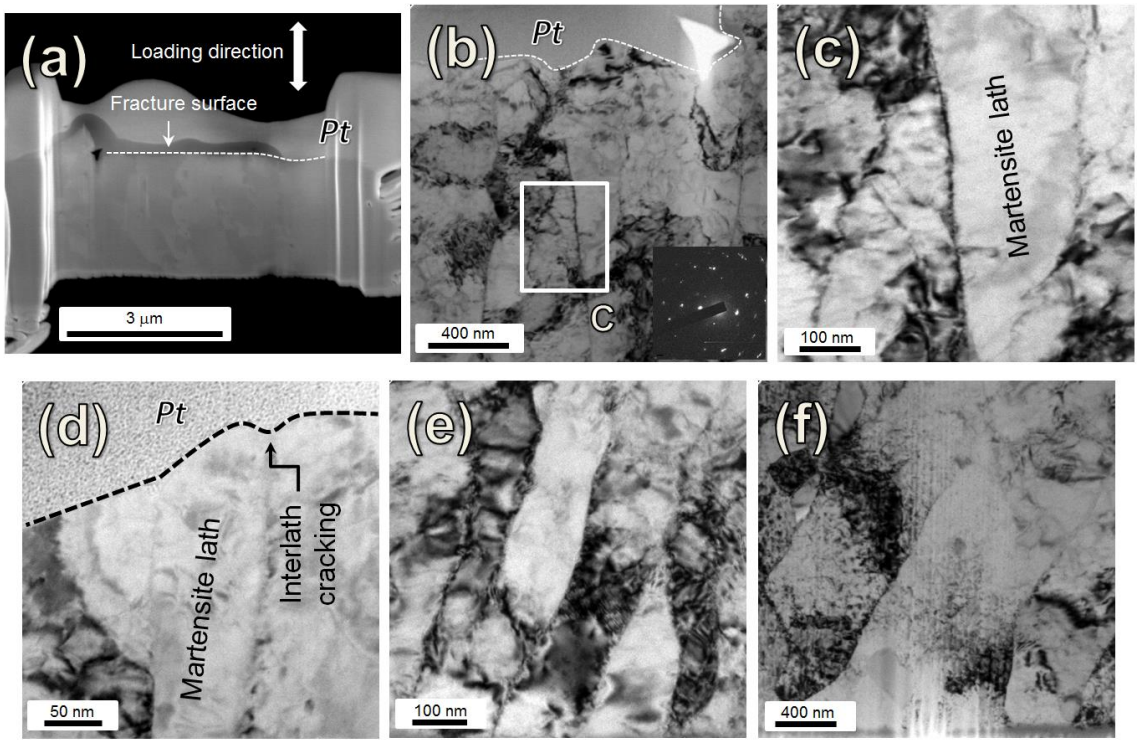
(a)
Loading direction
Fracture surface
Pt
3 μm
(b)
Pt
C
400 nm
(c)
Martensite lath
100 nm
(d)
Pt
Martensite lath
Interlath cracking
50 nm
(e)
100 nm
(f)
400 nm

Fig. 14

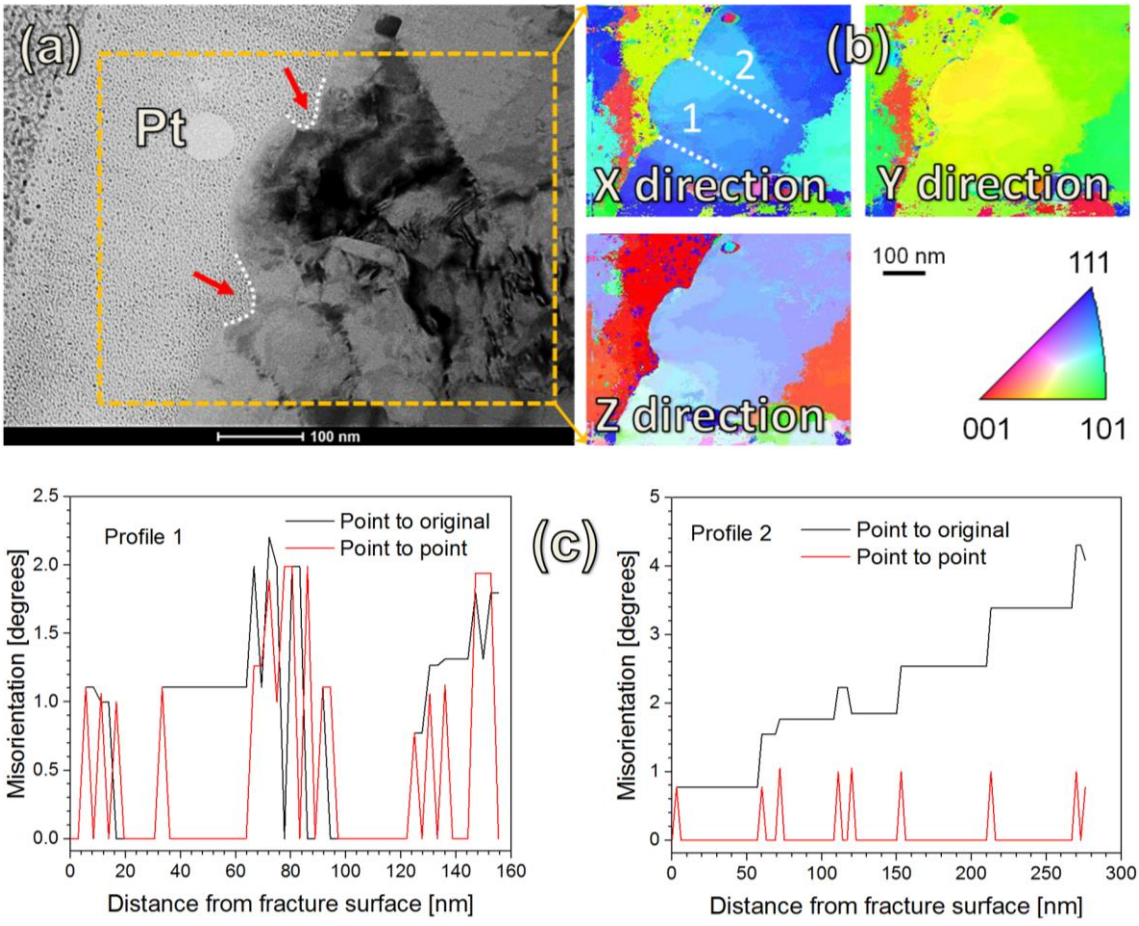
(a)
Pt
100 nm
(b)
2
1
X direction
Y direction
Z direction
100 nm
111
001
101
(c)
Profile 1
Point to original
Point to point
Misorientation [degrees]
Distance from fracture surface [nm]
Profile 2
Point to original
Point to point
Misorientation [degrees]
Distance from fracture surface [nm]

Fig. 15

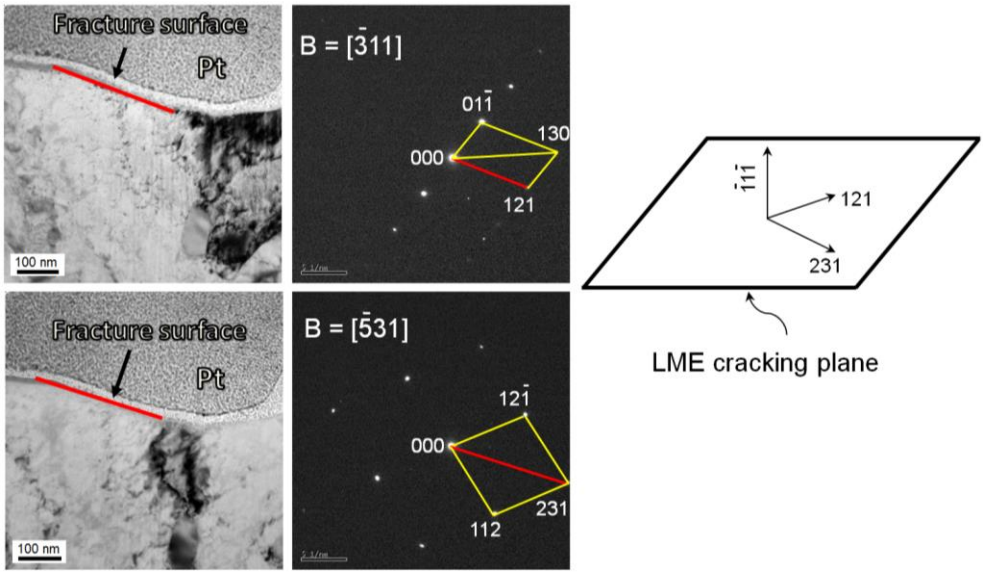
Fracture surface
Pt
100 nm
B = [3̄11]
011̄
130
000
121
Fracture surface
Pt
100 nm
B = [5̄31]
121̄
000
231
112
1̄11̄
121
231
LME cracking plane